A PRECONCENTRATING LAB-ON-A-CHIP DEVICE TARGETED TOWARDS NANOPORE SENSORS

KAITLYN KEAN

Thesis submitted to the Faculty of Engineering in
partial fulfillment of degree requirements for a

Master of Applied Science

In

Biomedical Engineering

Ottawa Carleton Institute for Biomedical Engineering

University of Ottawa

Ottawa, ON.

ABSTRACT

Continuous progress in the nanotechnology field has allowed for the emergence of powerful, nanopore-based detection technology. Solid-state nanopores were developed for next-generation sequencing and single-molecule detection. They are advantageous over their biological counterpart because they offer robustness, stability, tunable pore size and the ability to be integrated within a microfluidic device. With all of these attractive attributes, solid-state nanopores are a top contender for point-of-care diagnostic technologies. However, hindering their performance is an inability to distinguish between small molecules, pore-clogging, and the detection rate's dependence on sample concentration. The concentration-dependent detection rate becomes particularly evident at low sample concentrations (<1 nM), sometimes taking hours for the nanopore to sense a single molecule because of diffusion. The inability to distinguish between small molecules can be addressed using DNA nanostructures; however, pore-clogging and variable detection rates hinder its potential in a clinical setting.

This thesis proposes a microfluidic device design and methodology that seeks to mitigate pore-clogging and improve the detection rate for dilute samples. DNA coated microbeads will create a bead column within the microfluidic device and confine the target molecules to an extremely small (20 nL) volume. The sample can be washed, ridding the contaminants, and eluted on-chip, so the sample is purified and concentrated, affording a more reliable sensing performance. First, a magnetic microbead DNA assay was optimized off-chip, and the capture and release efficiencies were monitored using a Biotek™ Epoch™ 2 spectrophotometer (Chapter 2). Next, a novel microfluidic device design was optimized and validated to ensure precise sample manipulation (Chapter 3). Finally, the microbead assay was incorporated into the microfluidic device for sample concentration (Chapter 4). Fluorescence microscopy results suggest successful DNA elution from the microbeads within the microfluidic device, allowing for a 28.5 X concentration increase. This platform shows promise for sample preconcentration by reducing the starting DNA sample volume of 25 µL to 20 nL, which could improve the speed of solid-state nanopore sensing.

STATEMENT OF ORIGINALITY

The material herein presented is a direct result of my work as a master's student while under the supervision of Professor Michel Godin at the University of Ottawa.
In partial fulfillment of the requirements for the degree of Master of Applied Science: Biomedical Engineering, at the University of Ottawa, this work was presented at the Ottawa Carleton Institute for Biomedical Engineering Seminar Series:
Kaitlyn Kean and Michel Godin, A Preconcentrating Lab-on-a-Chip Device Targeted Towards Nanopore Sensors, March 2020.
A poster on this topic was also presented at the Engineering and Computer Science Graduate Poster Competition, March 2020.

STATEMENT OF CONTRIBUTION

The author wrote the entirety of this document. All figures and tables were created by the author unless otherwise mentioned in the caption. The author performed all the works presented, including device fabrication (photolithography and soft lithography), device testing, microbead assay testing, and data collection. Device design and photomask creation were done by a previous Post-Doctoral fellow in the Godin lab, Ali Najafi Sohi. The electrical setup and custom LabView® code for valve control were the works of a prior summer student in the Godin Lab, Kiran Naidoo-Edwardson.

ACKNOWLEDGEMENTS

Throughout my time as a master's student at the University of Ottawa, I have received a great deal of support and guidance. I would first like to extend my gratitude to my supervisor, Michel Godin. I cannot thank you enough for your patience, leadership, understanding and encouragement through this journey. Your insightful feedback pushed me to sharpen my critical thinking and brought my research to a higher level. The last six months of study have been challenging in light of the COVID-19 pandemic. Thank you for continuing to provide motivation, always making time for meetings and making sure the lab was a safe place for research.

I would also like to thank Dr. Ali Sohi for his selfless teachings and extremely valuable insight into this project. He set a strong foundation for me to build on. Even from California, while busy with his new career, he always answered my questions and provided encouragement.

Of course, I must mention Nicholas Soucy and Megan Dutcher, for, without their worldly conversations, humour and friendship, I might have gone crazy. After hours spent preparing for an experiment, only to have something go wrong, they were there for much needed moral support.

I would also like to recognize members of Vincent Tabard-Cossa's group for always being so welcoming and helpful. I must extend special thanks to Dr. Dan Tessier for his guidance while working with DNA assays. Thank you for taking the time to help me with calculations, protocols, ordering chemicals and keeping things in perspective when experiments didn't go as planned.

Finally, I must mention that none of this would have been possible without my family's support. Thank you, Dad, for instilling that anything is possible with hard work and dedication. Thank you, Mom, for always making sure I had home-cooked meals for "better brain function."

Lastly, and certainly not least, the person this thesis is dedicated to, my brother Garrett. Thank you for the late nights, being a perfectionist when I wanted to throw in the towel and doing your darndest to learn nanoscience with a background in distilling and biochemistry. You are no longer the most educated in the family; thank you.

LIST OF ABBREVIATIONS

- **ACL**: acceleration
- **bp:** base pair
- **CBD**: controlled dielectric breakdown
- **DAPI**: 4’,6-diamidino-2-phenylindole
- **DAQ**: Data acquisition
- **Isoelectric point**: pI
- **LOC**: lab-on-a-chip
- **LOD**: limit of detection
- **MoS_2:** molybdenum disulfide
- **PCR:** polymerase chain reaction
- **PDMS:** polydimethylsiloxane
- **PEG:** polyethylene glycol
- **qIPCR:** quantitative immuno-PCR
- **RFU:** relative fluorescence units
- **rpm:** revolutions per minute
- **SiN:** silicon nitride

TABLE OF CONTENTS

LIST OF TABLES

LIST OF FIGURES

Chapter 1 : Introduction

1.1 Nanopore Sensors: An Overview

Nanopore sensors are an up-and-coming biosensor with exciting potential. They offer a cost-effective, amplification free, high-throughput sensing method capable of single-molecule detection [1], [2]. With healthcare moving towards point-of-care methods and real-time diagnosis, nanopores have the potential to revolutionize existing technologies and improve disease detection, monitoring and treatment [3], [4].

1.1.1 The beginning of nanopore sensing

In the 1940s, Wallace H Coulter and his brother Joseph actualized an idea they had to count and size cells by passing them through an aperture [5]. The first cell counter Wallace Coulter created was made out of a cellophane wrapper that divided a glass container filled with an electrolyte solution. The cellophane wrapper had a tiny hole poked, and a set of electrodes were placed on each side of the wrapper, in solution, to create an electric current across the aperture. While monitoring solution conductivity, discrete, short pulses were observed when cells passed through the hole. A depiction of this process, later termed translocation, is shown in ***Figure 1-1 A***. They found the rate of the pulses correlated to the total number of cells in solution, and the magnitude of the pulses proportional to cell size [5], [6], giving rise to the first Coulter cell counter.

Nanopore sensing came to light in a notebook dating back to 1989 [7]. If the size of the aperture used in the Coulter-Counter can decrease from millimetres to nanometres, the sensing target could change from a single cell to a single molecule of DNA. By monitoring the conductivity, differences in pulses would be unique to each DNA base (A, G, T and C), could be used to determine a sequence of DNA (***Figure 1-1 B***)

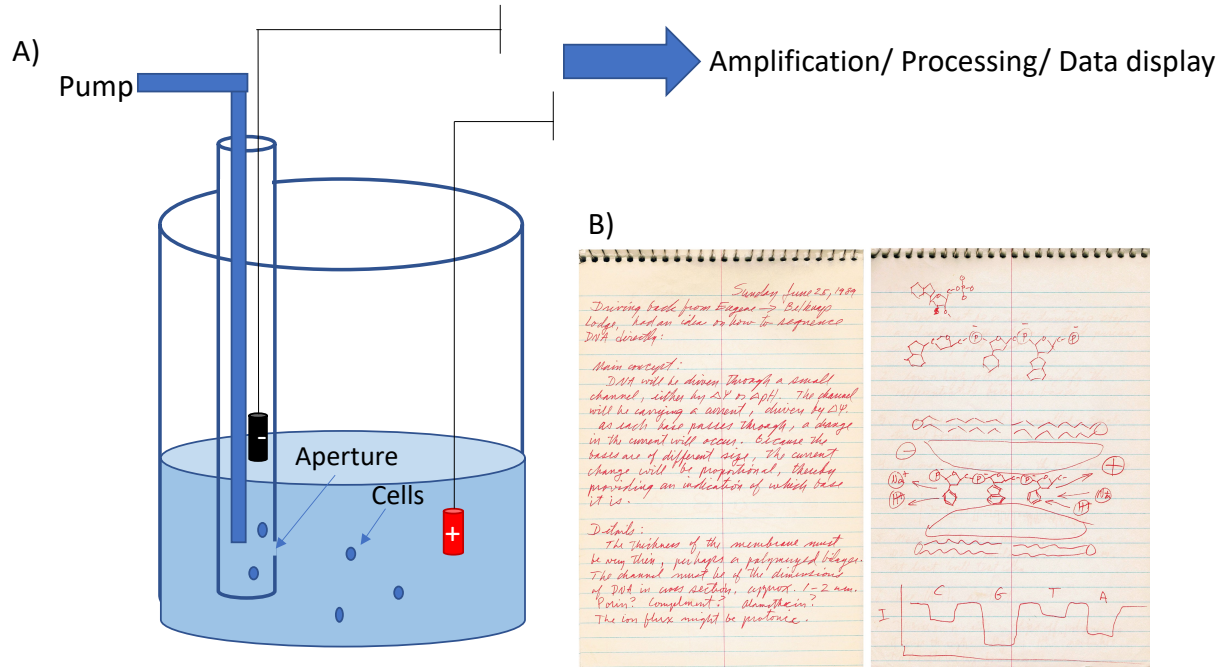

Figure 1-1: Coulter Counter schematic and conceptual drawings of a nanopore DNA sequencing. *(A) Coulter Counter; by initiating the flow of electric current through the aperture, a measurable decrease in current is observed as a particle translocates. (B) A conceptual diagram of a nanopore, based on the principles of the Coulter Counter, taken from D. Deamer's notebook. Images adapted from references* [6] *(A),* [7] *(B) with permission.*

1.1.2 Types of nanopore sensors

The first published nanopore experiments used biologically derived protein pores ***(Figure 1-2 A*)**. In the body, these pores are found in the lipid bilayer and perform functions such as maintain ion gradients and actively transport nucleic acids during different cell cycles. After years of research dedicated to improving biological nanopores, they achieved resolution at the atomic-level and are a platform for sequencing DNA [7], [8]. Unfortunately, biological nanopores suffer from extreme sensitivity to their environment, intrinsic instability and have a fixed pore size that typically only allows for single-stranded DNA to pass [4], [8]. Though capable of exceptional resolution, they are unfavourable for long term/multiple use or incorporation into nano-devices [1].

Solid-state nanopores were introduced to improve upon some of the limitations present in biological pores. They have a characteristic structure (***Figure 1-2 B***) and are fabricated in thin, synthetic membranes, such as silicon oxide [9], [10] and silicon nitride (SiN) [11], [12].

Fabrication has become quite cost-effective due to a recent pore formation method, namely controlled dielectric breakdown (CBD) [13]. Solid-state nanopores offer superior chemical and mechanical stability and can withstand a wide range of experimental conditions, such as changes in pH, voltages and temperature [2]. This enhanced robustness creates the potential to be integrated within lab-on-a-chip (LOC) and nano-devices [14]. Another upgrade is their ability to adjust the pore size, permitting them to detect a vast size of target molecules [15]–[17]. All of these advantages of synthetic membrane nanopores over the biological complements make an exciting area for exploration.

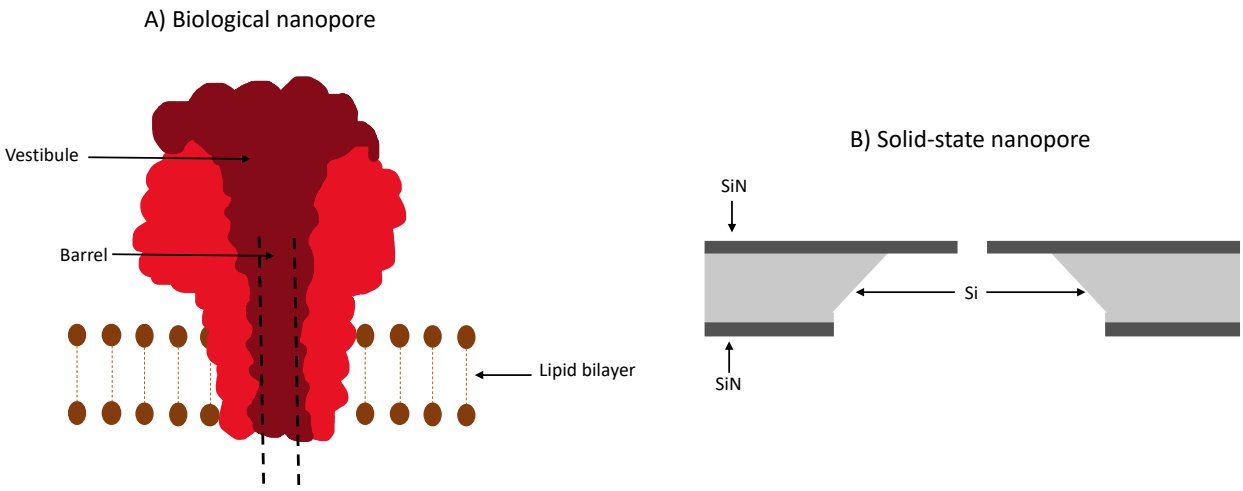

Figure 1-2: Cross-sectional view of nanopores. *(A) a biological nanopore embedded in a lipid-bilayer and (B) a solid-state nanopore fabricated in a thin, SiN membrane. Figure adapted from* [2] *with permission, not to scale*

1.1.3 Principle of nanopore sensors

Figure 1-3 depicts a typical nanopore device, sharing many similarities to the Coulter Counter described in Section 1.1.1, except on a smaller scale. The nanopore is fabricated in a membrane supported by a substrate immersed in a conductive electrolyte solution, dividing it into two chambers. When an electric potential is applied between these two chambers, an electric field is created across the pore. The nanopore is the only path for ions and charged biomolecules to translocate from one side to another [18].

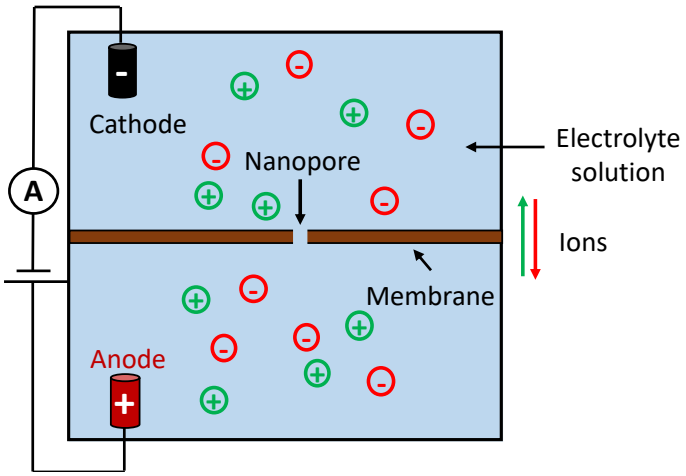

Figure 1-3: Schematic of a basic nanopore set-up. *The membrane separates two liquid compartments, allowing ion and fluid exchange. When a bias voltage is applied, electrolyte ions move through the nanopore. Figure adapted from* [3], [19].

Charged target molecules for nanopore sensing are typically DNA [20], RNA [21] and proteins [22]. Nucleic acids have a general structure that consists of three components: a phosphate backbone, a pentose sugar and a nitrogenous base. The negative phosphate backbone gives nucleic acids their acidic character and makes them excellent sensing targets for a nanopore [23]. The negatively charged nucleic acid is drawn, electrophoretically, across the pore towards the positive electrode, as shown in ***Figure 1-4 A***. Protein translocation is slightly different than nucleic acid translocation because proteins are amphiphilic molecules [23]. Proteins are made up of ionizable amino acids, so their overall charge is dependent on pH [23]. A protein's isoelectric point (pI) is the pH at which the protein's overall charge is zero. It is dependent on the amino acid sequence and post-translational modifications [23]. When the pH is lower than the pI, the protein's net charge is positive and will move through the pore towards the negative electrode [24]. When pH is higher than the pI, the protein is overall negatively charged and will move through the pore towards the positive electrode [24].

In a nanopore set-up, electrodes such as silver/silver chloride (Ag/AgCl) create a potential difference across the nanopore. When biomolecules translocate through the pore,

they temporarily block the ionic current, producing a measurable drop in baseline current (***Figure 1-4 B***). After translocation, the pore is empty, and the ionic current recovers to the baseline level. Each spike can be analyzed to determine the cross-sectional area and length of the molecule from the ionic current reduction, ΔI, and dwell time, t_{dwell}, respectively (***Figure 1-4 C***). These disruptions are unique, allowing nanopore sensors to detect subtle differences between molecules [25] and nucleotides [26].

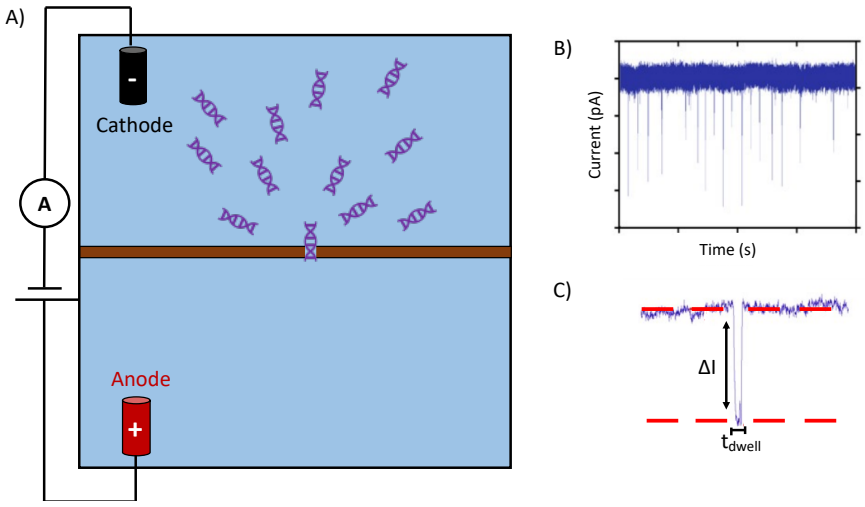

Figure 1-4: Biomolecule sensing schematic for a solid-state nanopore. *(A) Individual DNA molecules start passing through the nanopore (B) Electrical measurement traces of DNA molecules passing through a nanopore (C) Dwell time and blockage depth parameters used to determine molecule length and cross-sectional area, respectively. Source of data reference* [27].

Biomolecules translocating through a nanopore are strongly governed by applied potential (ΔV) and the geometry of the pore [28]. The measurement throughput of a nanopore is dependent on two things: the rate at which the target molecule arrives at the pore and the rate at which it enters the pore [29]. Most samples are at a low enough concentration that one can ignore the interactions between molecules so that the capture rate (*J*) is proportional to the concentration of target analyte (*c*).

$$J = Rc \qquad 1$$

Where *R* is the normalized capture rate that depends on the geometry of the nanopore and the electrophoretic transport properties of the target analyte [3].

The capture radius is a hypothetical semi-circle with radius r* outside the nanopore, as depicted in ***Figure 1-5.*** When the target analyte is at distances such that r > r*, it is freely diffusing in the bulk solution due to Brownian motion [30]. Therefore, the capture rate is limited by the time required for the target to arrive at the pore mouth (diffusion-limited). When the target analyte is at distances such that r < r*, it gets irreversibly captured and pulled toward the pore mouth. Under these circumstances, the effect of the electric field dominates the diffusive forces [31]. The size of the capture radius is dependent on many factors such as DNA length [32], experimental conditions [33], nanopore diameter [34] and applied bias voltage [32], [34].

Though the target molecule must be delivered to the pore mouth, it is only one piece of the puzzle. The other important piece is for the target molecule to enter the pore. An entropic barrier must be crossed to orient the molecule to enter the pore correctly (barrier-limited) [3]. Molecule detection and capture rates of a nanopore are predominately diffusion-limited, which creates a capture rate of 1 hZ/nM, indicating that the optimum concentrations for detection are on the nM (nanomolar) scale [33], [35]. When the target is present in a sample at a nanomolar level, a molecule can be detected every second and 500 molecules in about 8 minutes (**Table 1**). However, when the target is present in a sample at a picomolar level (10^{-3} nM), one molecule will be detected every 1000 seconds and 500 molecules in just under 6 days (**Table 1**).

Table 1: The effect of concentration on sensing time for solid-state nanopores (capture rate= 1 Hz/nM)

Sample concentration	Time to sense 500 molecules
µM	0.5 seconds
nM	500 seconds
pM	6 days
fM	> year

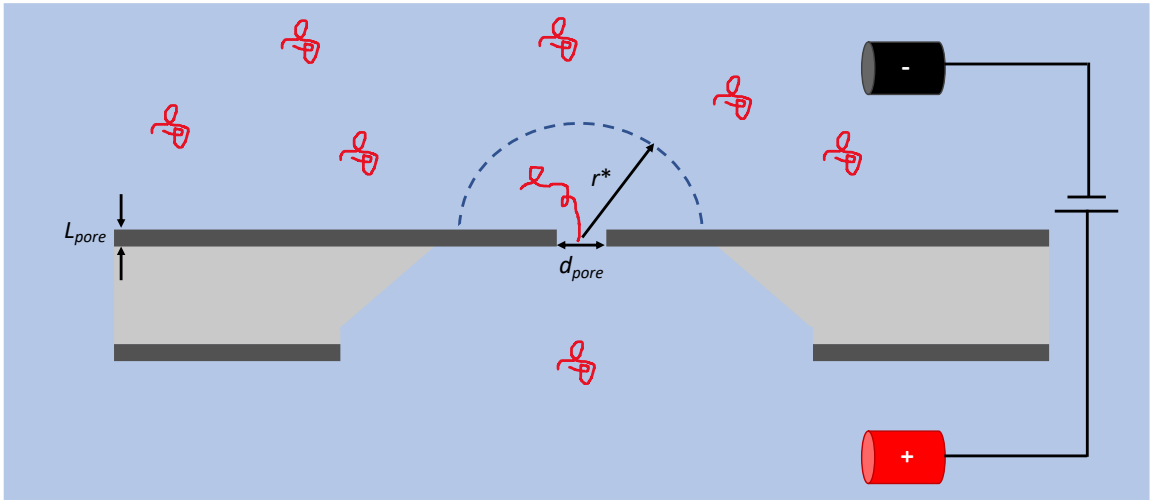

Figure 1-5: Biomolecule capture by a solid-state nanopore when a bias voltage is applied (not to scale). *The capture radius, r*, is a hypothetical semi-circle around the nanopore. The electric field is negligible at distances far from the pore (r*<<r), and molecules move in a diffusive fashion. At distances smaller than r*, the electric potential drives molecules to the pore. Figure adapted from* [3].

1.2 Biomarkers for Disease Detection

Biomarkers are biomolecules that can indicate the presence and severity of disease processes and give insight into response to treatments. Many life-threatening conditions start at clinically undetectable levels of biomarkers and steadily increase until symptoms arise [36]. The earlier a disease or illness can be identified, the better chance of curing, treating and reversing the damage. Advances in molecular diagnostics and screening technology have improved our ability to identify disease-specific genomic, proteomic, and epigenetic signatures [37]. This has led to the identification of biomarkers that can detect disease and illness early in their development. Biomarkers can take many forms, including DNA [38], RNA [39], protein [40] and lipids [41]. The ultimate detection platform for these biomarkers would be inexpensive, non-invasive and allow time for effective intervention.

1.2.1: Understanding current detection limitations

Attractive, non-invasive methods for extracting biomarkers from the body include taking blood, urine or saliva samples. However, disease biomarkers in these types of samples are often extremely dilute and mixed with many other biomolecules, making their detection difficult [42]. The ability to increase the concentration of target analytes in a fixed sample volume can lower the detection limit for many biosensing platforms [43]. Polymerase Chain Reaction (PCR) based diagnostics is one of the most potent tools today to increase target DNA concentration. The DNA of interest can be replicated numerous times through PCR, amplifying it significantly, making detection much more reliable. The method relies on knowing the sequence of target DNA responsible for the disease [44]. Identifying the target sequence can be expensive and time-consuming, two significantly limiting factors towards point-of-care diagnostics.

In some cases, protein biomarkers are simpler to identify [45]; however, they are still fairly dilute in non-invasive serum samples, and PCR amplification does not work on proteins [42]. Some other, more versatile methods for increasing biomarker concentration include sample evaporation, dielectrophoresis, column chromatography and magnetic bead-based separation [46], [47]. Concentration by evaporation works by vaporizing the liquid to gas, leaving the biomolecules in a more concentrated sample [48]. Dielectrophoresis is the motion of particles in a non-uniform electric field [49]. It can concentrate particles of interest to a focal point by exploiting certain field conditions [49]. Column chromatography uses interactions between different molecules to isolate the biomolecule of interest [50]. The target is adsorbed in the column, while molecules that aren't of interest are washed out. Increasing the target concentration occurs during elution from the column by decreasing the volume of elution buffer. Magnetic beads can be mixed in the sample to capture target biomarkers, recollected magnetically, and the target can be released under favourable conditions [51]. Depending on the volume of elution buffer, a concentration increase is achievable [52]. Column chromatography and magnetic bead separation can integrate antibody/antigen selectivity [53], [54], making them attractive options for selectively increasing sample concentration.

1.2.2: Current biomarker detection

The potential to diagnose and monitor diseases by detecting the presence of biomarkers is an exciting possibility. Two state-of-the-art technologies for detecting biomarkers are Single Molecular Arrays (Simoa™) from Quanterix Corp. and Immuno-PCR (IPCR) on the Imperacer ® platform from Chimera Biotec GmbH. The Simoa™ digital ELISA from Quanterix Corp. has shown promise for detecting extremely low concentrations (fg/mL) of biomarkers[52]. Biomolecules are captured on microscopic magnetic beads, and each is fluorescently labelled. The beads are introduced to a disc with an array of femtoliter-sized wells; each well can only accommodate one bead [55]. Then Simoa uses a unique signal detection system to detect the number of biomolecules stuck to a bead. Each target analyte encounters a bead in less than 1 minute [56]. Simoa™ offers faster data acquisition, multiplexing up to 10 different analytes and can detect low concentrations where conventional methods hit their limit of detection (LOD) [57]. It also offers full automation-including sample dilution, mixing, washing, incubation and data acquiring steps. In the last few years, there has been a push to miniaturize this technology using digital microfluidics and microbubbles [52].

Quantitative mmune-polymerase chain reaction (qIPCR) can detect specific antigens using antibodies labelled with double-stranded DNA [58]. The DNA is amplified downstream by quantitative PCR for a more robust signal. The amplification allows qIPCR to detect low biomarker concentrations, 100 fg/mL – 10 pg/mL [59]. The Imperacer® is not automated at this time and, like most systems of this nature, require trained personnel. A qIPCR assay requires between 4-7 hours [60] and is not down-scalable [61], hindering its application in POC settings.

1.2.3: Nanopore's potentials and limitations in disease detection

State-of-the-art platforms mentioned above use fluorescent signals and complex optics to analyze a sample. Nanopores offer a different approach to biomarker detection because the signal generation is solely based on changes in the current [62]. Various infectious diseases, including Ebola [63] and Lassa fever [1], [64], have been diagnosed through DNA and RNA

sequencing using Oxford Nanopore's MinION sequencer, which is based on biological nanopores [1]. The potential of solid-state nanopores in disease diagnosis is still unknown, but because of the benefits they confer (1.1.2 Types of nanopore sensors), this area is now being heavily researched.

For solid-state nanopores to compete with current biosensing technology, two limitations must be addressed: low resolution leading to poor selectivity [65], [66] and low reliability [67]. Limitations of resolution stem from the thickness of the nanopore membrane (spatial resolution) and extremely fast translocation of target molecules through the pore (temporal resolution). Thinner membranes need to be fabricated to increase the spatial resolution of solid-state nanopores [68]. The thickness of a conventional SiN membrane is about 20-60 times larger than the gap between DNA base pairs, which is about 0.3nm [68], [69]. This difference means 20-60 nucleotides are in the pore at one time, reducing the nanopore's ability to distinguish between the sequences of similar length DNA [1]. The ultimate goal is a membrane with a thickness of 0.3nm to achieve single base-pair resolution. Molybdenum disulfide (MoS_2) [70] and SiN [71] have shown the feasibility of this type of resolution. There are two approaches to improving temporal resolution issues: slowing the translocation of biomolecules [72] and increasing data acquisition [73]–[75]. A single molecule's translocation time is often shorter than the measurement time interval of the acquisition system [74]. This acquisition lag means molecules pass through the pore unaccounted for, or they distort the raw data if partially detected [73]. Slowing the translocation of biomolecules is a more affordable solution [76]. Slowing translocation also rivals the goal of high throughput sensing, so increasing data acquisition is a more favourable long-term approach.

There are a few techniques that have been developed to address the resolution shortcoming and increase selectivity, including modifying experimental conditions [65], [77], [78], using optical or magnetic tweezers [79], electrical gating [80] and using DNA nano-switches [72]. Many of the options introduce complexity to the device design [72]. DNA nano-switches not only slow the translocation speed but can also act as a label to distinguish between molecules, permitting specific molecule detection with minimum complexity [81].

The idea is to strategically attach the molecule of interest to a long strand of DNA to trigger a conformational change (***Figure 1-6***). These changes can be achieved by manipulating strong interactions, such as antigen/antibody, biotin/streptavidin, or hybridizing pieces of DNA or RNA together [81]. The new, unique molecular structure is distinguishable from the electrical traces, increasing resolution and selectivity [72].

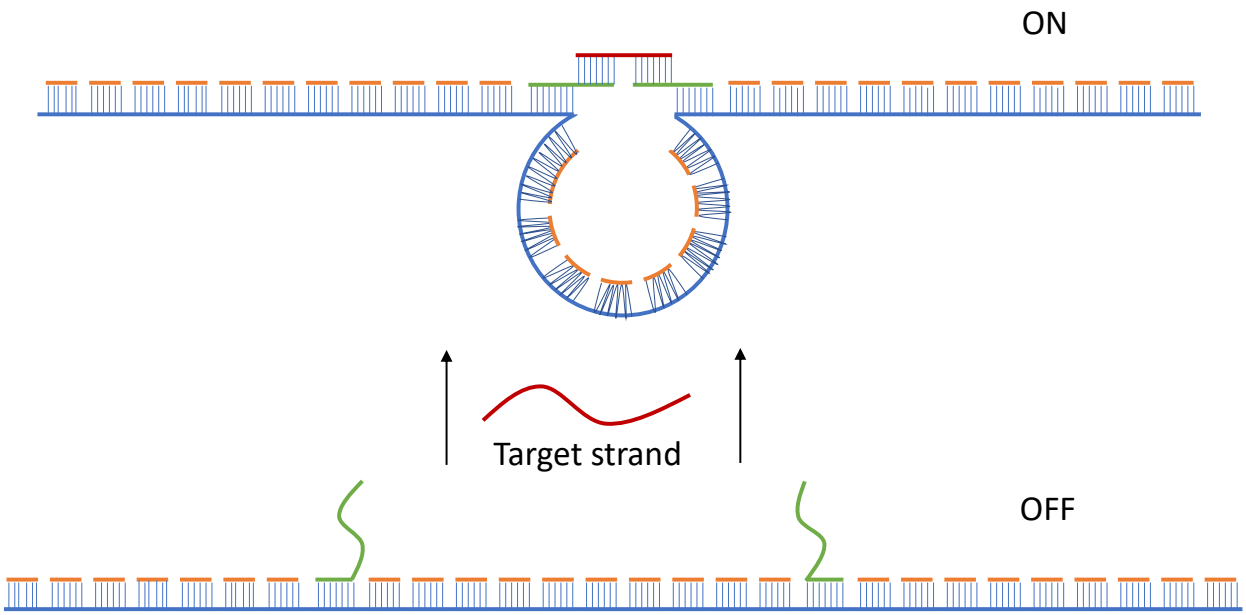

Figure 1-6: DNA nanoswitch schematic. *A change in conformation occurs to the ssDNA when the target gene is present and bonded to its complementary sequence. Figure adapted from* [52]

Apart from improving the resolution in solid-state nanopores, the device's reliability also needs to be addressed. Nonspecific adsorption of biomolecules onto the nanopore's membrane or wall and variable detection rate diminishes the device's reliability and usability [82]. Undesired adsorption can produce erroneous signals [83]. It can also block target molecules from translocating and cause temporary or permanent damage to the device [84]. One approach to solve unwanted adsorption is to coat the nanopore membrane with an anti-sticking agent, such as polyethylene glycol (PEG) [67] or lipid coatings [85].

The detection rate of solid-state nanopores is exceptionally dependent on the sample's concentration, hindering its real-world applications. As mentioned earlier, their optimum sensing range is on the nanomolar scale [82], [86]. When concentrations are below this, the detection rate drops significantly, and measurement times can become quite lengthy (> 1hr) [33], [35]. A few methods have been employed the rectify this, such as single-molecule dielectrophoretic trapping [33], using asymmetric electrolyte solutions on either side of the pore [31] and precisely controlling the temperature near the pore [87]. Though effective at increasing the nanopore's dynamic range, these solutions are not ideal for more complex biological samples as they don't offer any selectivity [88].

1.3 Objectives

This project aims to improve the time-to-response of solid-state nanopores for low concentration samples while improving sample purity. Thus, magnetic bead-based separation and microfluidics were combined, which increases concentration through volume reduction. A novel microfluidic device was designed and fabricated, capable of trapping magnetic microbeads, washing impurities, mixing and eluting. Pneumatic push-up valves achieve all fluidic manipulations on-chip. The beads are trapped by a sieve valve that closes partially to allow fluid to pass but catches the beads, forming a column within the fluidic channel. Peristaltic pumping pneumatic valves perform on-chip mixing. The beads are confined to a closed-loop of ~20 nL, where the target is eluted off the beads. This method affords a concentration increase of 28.5X. The ground-breaking concentration capabilities show promise for improving the detection of dilute samples by solid-state nanopores.

This project was tackled in three different steps, which are represented as the chapters of this thesis. The first step, outlined in : Magnetic Microbead Assays (Off-Chip), involved quantifying magnetic microbead assays and tweaking the protocols to be compatible and optimized for the microfluidic device. The next step, : Validation of a Microfluidic Device, outlines how the microfluidic devices were characterized before incorporating the microbeads. The final step, described in : Incorporating Microbead Assays with a Microfluidic Device,

involved combining efforts one and two, building an on-chip microbead concentration column and elution of the DNA from the beads into a much smaller volume, to increase the concentration. It is worth clarifying that on-chip refers to the experiment being carried out on the microfluidic device. Off-chip refers to the experiment being performed in a centrifuge tube.

Chapter 2 : Magnetic Microbead Assays (Off-Chip)

2.1 Motivation and Objectives

Solid-state nanopores suffer from low specificity and lengthy time-to-response when detecting dilute target molecule samples (< nM), as discussed in Section 1.2.3: Nanopore's potentials and limitations in disease detection. Many circulating biomarkers are below this range [59], [89], [90], and similar in size [91], highlighting the need for a method that concentrates a target analyte before nanopore detection.

Magnetic beads are a standard tool used to capture and release target molecules. This technique for the separation of biomolecules is efficient, easy, and affordable [92]. Another bonus to this approach is that the bead size and coatings can be specific for the application and target analyte. This selectivity is not realized when using other concentrating methods such as evaporation or dielectrophoretic trapping [93]. The goal of this chapter is to characterize a few microbead protocols in centrifuge tubes (off-chip). Analyzing the bead capture and release efficiency gives insight into the concentrating viability of this method. This chapter compares two protocols and the trade-off between DNA recovery and microfluidic device complexity.

2.2 Introduction

Separation and concentration of biomolecules are essential steps in many biochemical and diagnostic processes. Many downstream applications such as detection [94] and sequencing [93], [94] cannot be performed using the unpurified sample. The presence of large amounts of cellular contents or other contaminants often impedes the quality of results given by these downstream applications [95]–[97]. Solid-phase purification is used in many commercial extraction kits because it is quick and efficient [56], [98]. Typically, solid-phase extractions consist of four steps: cell lysis, biomolecule adsorption, washing and elution [98]. It often relies on a spin column with centrifugal forces to separate the target from the rest of the sample [52]. These methods are not only time consuming because of sample preparation, but they also suffer from column clogging, require the use of a pump system, and are unable to accommodate large sample volumes [55]. Magnetic solid-phase extraction has become one of

the most useful and powerful techniques for separating biomolecules because the problems mentioned above are avoided [56].

2.2.1 Magnetic solid-phase separation

Magnetic solid-phase separation uses functionalized magnetic particles to adsorb target analytes and an external magnetic force for easy separation (***Figure 2-1***) [52], [57]. This method's two advantages over traditional solid-phase extractions are that target molecule capture can be done from a crude sample [52], and disruptive centrifugation steps are not needed [55]. Magnetic separation techniques are compatible with a wide range of sample volumes and concentrations, and their functionality can be altered to isolate a wide range of target biomolecules [52].

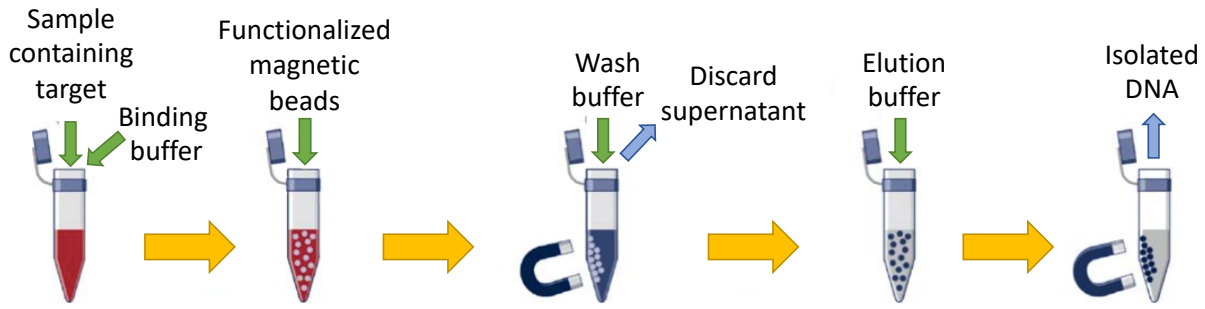

Figure 2-1: Magnetic bead solid-phase separation schematic. *Functionalized magnetic beads bind to the target in the sample. A magnet collects the beads so that the supernatant can be removed. After washing steps to remove contaminants, the target is released from the beads in an elution buffer. Figure adapted from* [52] *with permission.*

The surface functionality of magnetic particles is responsible for their unique properties that are imperative for isolating specific targets [99]. Many different biological applications have been realized due to magnetic beads' functionalization, one of the most critical being biomarker isolation. Other coatings can be used depending on the type of biomolecule being isolated and the degree of selectivity required. Silica is the most common material used to isolate DNA from a sample [100]. At a neutral pH, amorphous silica possesses a negative charge, and DNA adsorption is not electrostatically favourable [100]. However, in the presence of concentrated chaotropic salts, such a guanidium thiocyanate, DNA adsorbs to the surface of

silica [101]. The other molecules remain in the solution and are removed from the sample. This mechanism is still not fully understood, but it is well accepted that there are three main competing effects [100], [102]. 1. Chaotropic salt shields the negative charges to weaken electrostatic repulsion between silica and DNA. 2. Dehydration of DNA and silica in the presence of chaotropic salts. 3. Intermolecular hydrogen bond formation. After washing the beads to remove the salt and other impurities, DNA is eluted using a low salt buffer. Buffers without chaotropic salts are also successful at isolating DNA [101]. The electrolytes in the buffer shield the electrostatic repulsion and facilitate adsorption by forming a cation bridge between the dehydrated DNA and silica [102], [103].

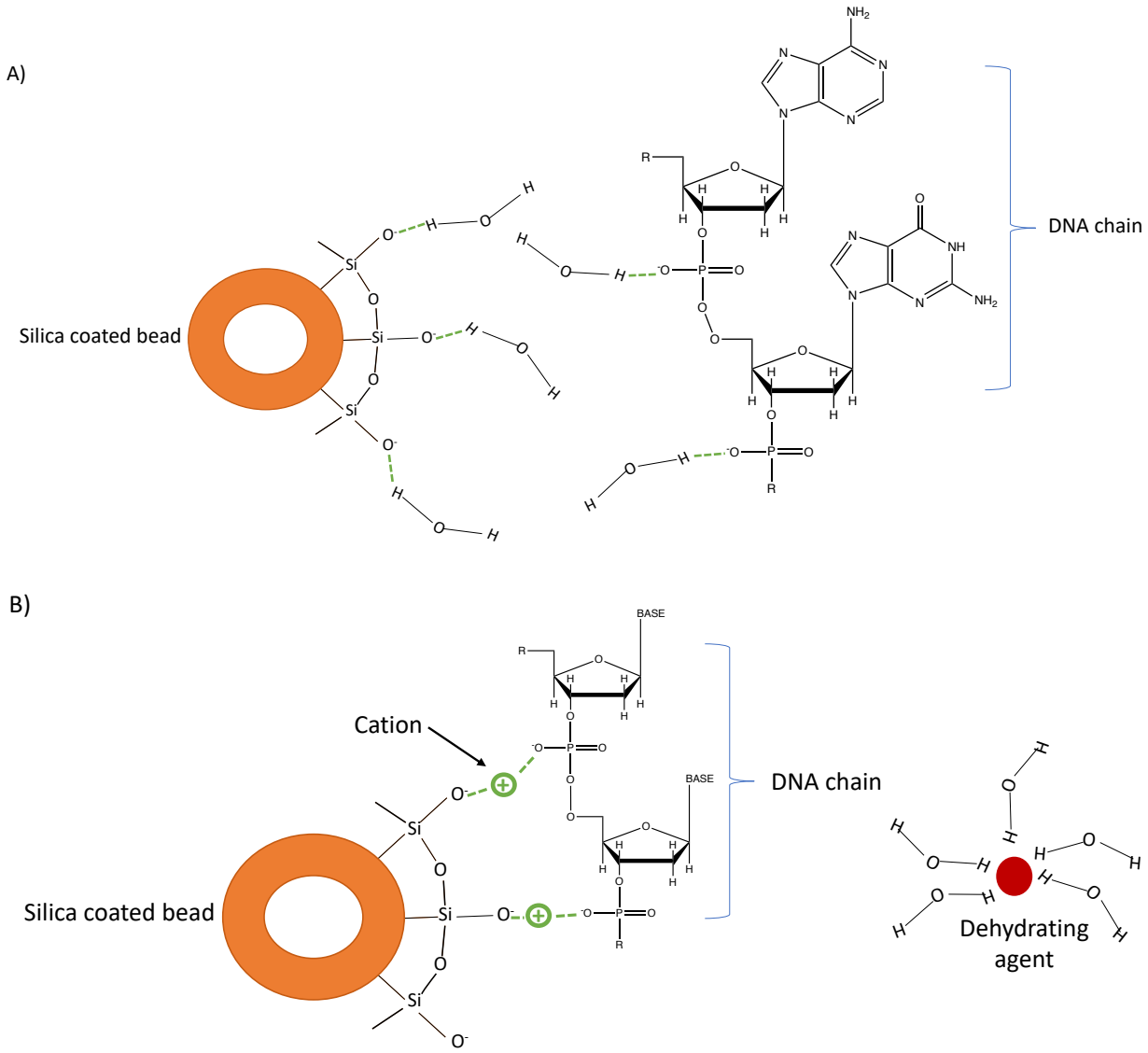

Figure 2-2: Mechanism of DNA adsorption to silica. *A) Under normal, low salt conditions, both the DNA and silica are hydrated and do not interact. B) In the presence of a dehydrating agent (can be chaotropic salt), the water surrounding the silica and DNA backbone is removed, and a cation facilitates the adsorption of DNA to silica by shielding the electrostatic repulsion.*

Silica and carboxyl groups have negatively charged oxygen at a neutral pH [100], [104]. Silicon and carbon are in the same row in the periodic table. Being from the same group in the periodic table means they have the same number of electrons in the valence shell and tend to react the same way with other substances. Carboxyl-coated magnetic beads are also known to have DNA isolation capabilities [105], probably through a similar mechanism to that proposed for silica.

There are many different surface modifications for magnetic beads, depending on the application [100], [106]. The versatility of magnetic beads means this approach to concentrating a sample is not limited to one specific disease; as long as there is a bead assay, concentration can be achieved. In this work, the binding and elution capacity of carboxyl-coated magnetic beads was studied. Theoretical calculations were compared to experimental results to determine the success of molecule isolation. These results are used to help quantify the success of the assay when performed on-chip.

2.3 Experimental

2.3.1 Capture and isolation of target DNA using COOH coated magnetic beads

DNA (No Limits 50 bp DNA fragment) at a concentration of 30 ng/µL in 25 µL of diH2O (distilled water) was mixed with 5 µL of MagSi-DNA 3.0 COOH microbeads* (3 µm diameter) were mixed by vortex in a chilled binding buffer (99% ethanol, 8 mM magnesium sulphate). The binding buffer was chilled to accelerate precipitation. The mixture was incubated on ice for 10 minutes, agitating every few minutes and then placed on a magnetic separator until all the beads were collected to the magnet (3-5 minutes). The supernatant was removed and placed in a separate microcentrifuge tube for later analysis of capture efficiency. The beads were then washed in 100 µL of chilled binding buffer two times before elution. Elution took place in either 25 or 10 µL of low salt buffer (diH_2O). The sample was incubated at either 56℃, on a hot plate, or at room temperature (~22℃) for 10 minutes, agitating every few minutes. The sample was placed on the magnetic separator until the beads were collected. The solution was carefully removed, ensuring beads were left in the tube and placed in a separate microcentrifuge tube for analysis.

*Calculations for the volume of microbead solution to add can be found in the **Appendix**.

2.3.2 Quantification of bead captured DNA concentration

The concentration for all samples was measured using UV absorbance (BioTek™ Epoch™ 2 Microplate Spectrophotometer). The number of DNA molecules in eluted samples and starting samples was compared to determine the beads' efficiency of DNA isolation.

2.4 Results & Discussion

2.4.1 Microplate spectrophotometric analysis

DNA samples eluted in 25 µL were analyzed using Biotek™ Epoch™ 2 Microplate Spectrophotometer in replicates, and the results are shown in ***Figure 2-3***. When elution was performed at room temperature (22℃), 40.4 ± 6% of the DNA from the starting sample was recovered in the eluant. Comparatively, when elution was performed at 56℃, 46 ± 3% of the DNA from the starting sample was recovered in the eluant. When the supernatants at both temperatures were analyzed, 20-30% of starting DNA remained in solution and was not captured by the beads. The wash solutions were also analyzed, but DNA content was undetectable. The limit of detection for the Biotek™ Spectrophotometer is 1.2 ng/µL dsDNA [107]. About 30% of initial DNA is unaccounted for, some may remain attached to the beads after elution, and some loss can be attributed to random error. Heating the sample during elution recovers more DNA with better consistency; however, having to heat the chip would add complexity to the final device set-up. Elution at room temperature achieves a similar recovery ratio and would not require a more complicated set-up.

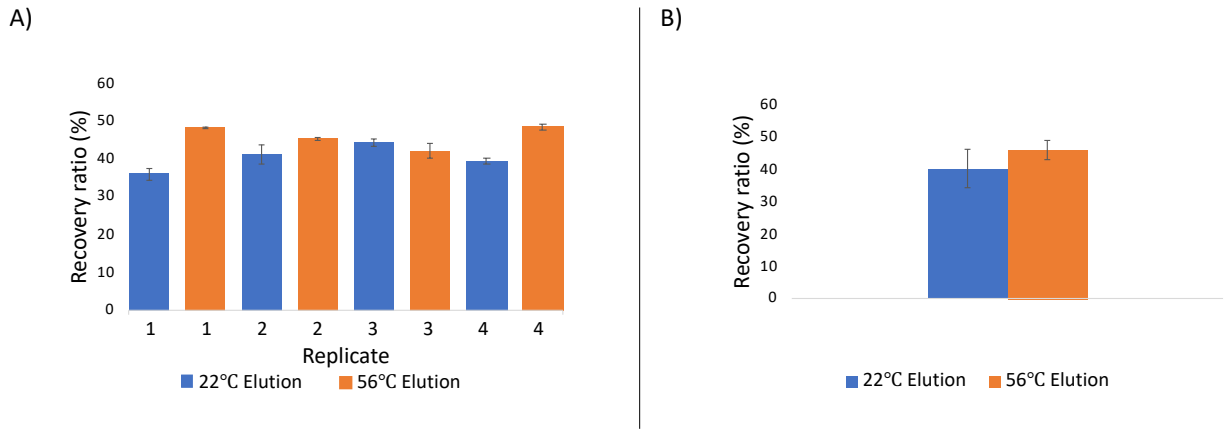

Figure 2-3: Relative recovery of DNA. *Elution performed at 22 ℃ recovered an average of 40.4% of the original DNA ((B) blue bar). Elution performed at 56 ℃ recovered an average of 46% of the original DNA ((B) orange bar).*

Bordelon *et al.* used Dynabeads® MyOne™ Silane magnetic beads (1µm diameter) to isolate a tuberculosis DNA sequence from spiked urine samples [51]. They report recovering 58% of DNA when using a 140bp segment but only 10% for a 75bp segment. Literature shows a decrease in nucleic acid extraction efficiency as the length of DNA becomes shorter [51], [108]. For DNA segments between 50-100bp, most methods extract less than 20%, and results are sporadic [108]. This is probably due to there being fewer base pairs forming a link to the bead surface, so the interaction is weaker. The size of DNA fragments should be considered when choosing an extraction method. Larger sized DNA fragments (>100 bp) would be more suitable for this method of isolation.

2.4.2 Bench-top method for increasing concentration using magnetic bead isolation

DNA samples were eluted in a smaller volume, 5 µL, to investigate the practicality of using bench-top methods to increase concentration through volume reduction. 5 µL was chosen as it is the smallest volume that still affords replicates on the microplate spectrophotometer. Eluted samples were analyzed spectrophotometrically in replicates, and the results are shown in ***Table 2***. The average concentration increases calculated from results in ***Table 2*** was 1.5X ±0.3. A 2X concentration increase should have been attained based on the 40% recovery achieved above, so these results are reasonably agreeable. The variability seen in the third column of ***Table 2*** (concentration increase) could stem from the difficulty in removing all the binding buffer prior to elution. The binding buffer is high salt for DNA binding, and the

elution buffer needs to be low salt for the release of DNA. If not all of the binding buffer was removed, this would increase the salt concentration of the elution buffer, decreasing the efficiency of DNA release, leading to variability in the results.

Table 2: Benchtop method concentration increase

Replicate number	Average concentration (ng/ µL)	Concentration increase
1	9.594	1.9
2	7.123	1.4
3	6.569	1.3

Bordelon *et al.* report a 10-fold concentration increase using magnetic beads [51]. They started with larger sample volumes (1-5 mL), which makes reducing the volume by bench-top methods more feasible. Some more investigation needs to be done to determine the largest starting sample volume and smallest elution volume to yield the greatest biomarker concentration increase. However, these experiments' goal was to highlight the need to manipulate smaller volumes of fluid to increase concentration.

2.5 Conclusions

Characterizing these beads' capture and release efficiency is essential to ensure that they function the way they were intended. This becomes a necessary step for comparison when they are used in later chapters. The results indicate that the capture efficiency for MagSi DNA 3.0 COOH increases ~6 % when elution is performed at 56℃, the recommended temperature. However, incorporating a heating method into the microfluidic set-up poses some complications that can be avoided. Assuming elution at room temperature remains consistent at ~40% DNA recovery when elution is performed on-chip, a significant concentration increase can still be achieved.

The concentration increase that is feasible when starting with small sample volumes (µL scale) is limited when using bench-top pipetting methods. In order to start with a larger sample

volume that contains the same number of molecules used in this section ($1.4x10^{13}$ copies), a longer incubation for DNA binding would likely be required to account for diffusion, and this should be investigated. In a centrifuge tube, using very careful and tedious pipetting skills, concentration increases of ~1.5X were achieved using MagSi DNA 3.0 COOH microbeads. A significant improvement is required to capture clinically relevant biomarkers (picomolar and lower) and increase their concentration level for optimal nanopore sensing.

Chapter 3 : Validation of a Microfluidic Device

3.1 Motivation and Objectives

Microfluidic platforms show excellent compatibility with nanopore sensors [109]. They have an unmatched ability to manipulate small (nL) sample volumes, potentially reducing sample consumption significantly and increasing the detection efficiency of the nanopore [19], [110], [111]. Microfluidic systems provide a clean, fresh sample delivered to the nanopore through constant flow and presents the option for a parallel, portable detection scheme [109]. On-chip preconcentrating devices offer a logical solution to the detection rate limitation and adds purification capabilities to solid-state nanopore platforms. This chapter describes the validation process of a novel microfluidic device before incorporating microbead assays.

3.2 Introduction

3.2.1 Introduction to microfabrication

Microfluidic LOC methods were initially targeted towards developing integrated, miniaturized devices that performed bench-top functions [112]. In recent years, these LOC methods have begun to specialize in single-molecule analysis because of the ability to incorporate solid-state nanopores within microfluidic devices [112]. A few advantages of integrating solid-state nanopores with microfluidics is manipulating, trapping, counting, and analyzing individual molecules on a massively parallel, miniaturized device [113]. On top of operational advantages, device fabrication is relatively facile and inexpensive, experimental set-ups are straightforward, and reagent consumption is exceptionally low [113].

Microfluidic prototyping can be broken down into two main steps: creating the master mould and replicating it into a polymeric microfluidic device. The construction of the moulds and assembly of the microfluidic devices must occur in an extremely clean, dust-free environment, called a cleanroom. The environment's humidity and temperature are regulated continuously to ensure proper conditions while creating extremely fine features. Master moulds are generally made using a process called photolithography. The procedure involves coating a substrate with a photosensitive resist then exposing it to a UV light source through a

mask with the desired design features. The areas exposed to the UV light either cures or solubilizes depending on the photoresist used [114]. There are two types of photoresist: positive and negative. When using a positive photoresist, the areas exposed to light become soluble and wash away in the photoresist developer ***Figure 3-1***.The areas exposed to light when using a negative photoresist cure and the unexposed regions wash away in the photoresist developer (***Figure 3-1***). SU8- series made by MicroChem (MA, USA) and AZ-series from Integrated Micro Materials (TX, USA) are the two most common photoresists. SU8 are negative photoresists that create square-shaped features with high resolution. AZ, on the other hand, are positive photoresists and when reflowed (an extra heating step at the end of fabrication), the features become rounded instead of squared [115]. These rounded channels are more favourable to obtain a tight seal when pressurized control channels (valves) are fully compressed [114].

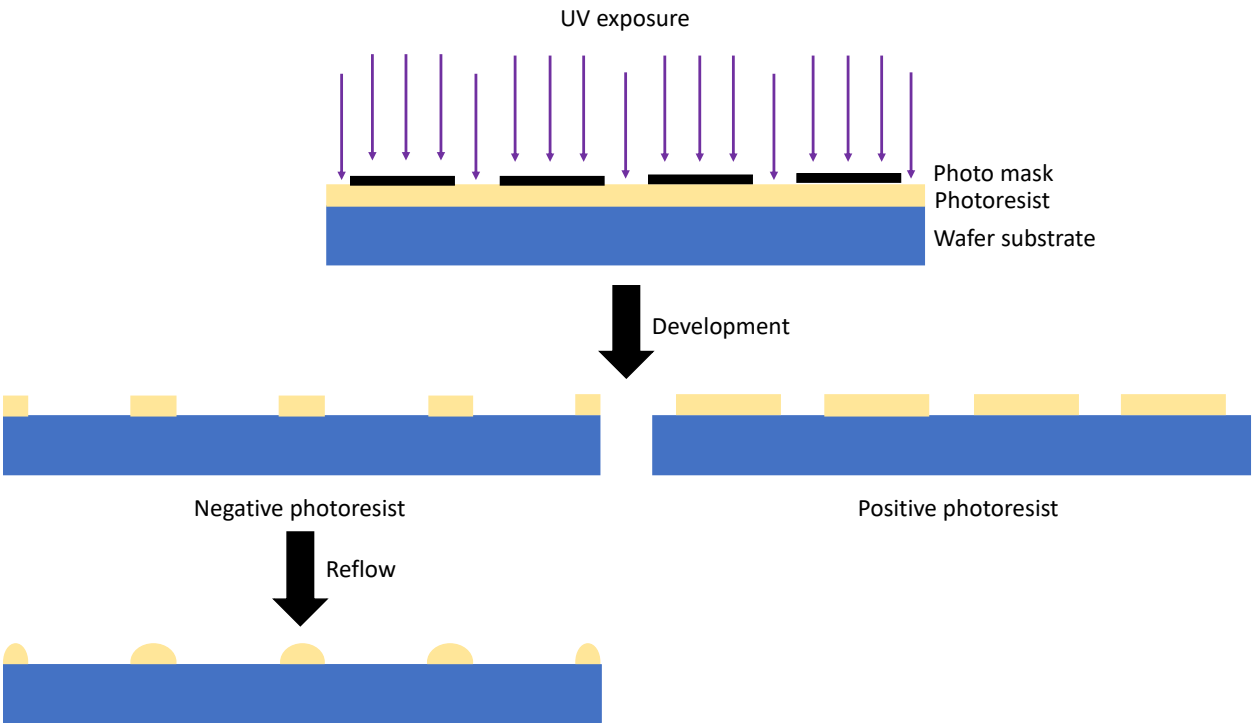

Figure 3-1: Process of photolithography using different types of photoresist. *After UV exposure and development, the areas exposed to UV either cross-link and become the features (negative photoresist) or dissolve, and the unexposed regions become the features (positive photoresist)*

A silicon wafer usually is the substrate coated with photoresist. A process termed "spin coating" is used to achieve the desired thickness of photoresist on the wafer [114]. The wafer is then soft-baked to evaporate the solvent and thicken the resist. A transparent sheet with printed patterns is placed in contact with the wafer and selectively exposed to UV for optimal cross-linking. A post bake step is done to promote cross-linking of the features. Finally, the wafer is submerged in the appropriate developer to remove all uncured photoresist. If rounded features are desired when using a negative photoresist, a heating step at the end termed 'reflow' is required. Fabrication parameters, including spin speed, bake temperature and length, amount of UV exposure and time and development technique, are specific to each device and each photoresist [116].

The second step in microfluidic prototyping involves replicating the master moulds in PDMS (polydimethylsiloxane), using soft lithography. Multiple layers of PDMS moulds can be bonded

together or to glass slides using plasma treatment. Plasma treatment changes the methyl groups (Si-CH_3) to hydroxyl groups (Si-OH) on the surface of the PDMS [117]. When two plasma-treated PDMS surfaces are brought together, a covalent siloxane bond (Si-O-Si) forms [117]. Two-layer devices are often used to create on-chip valves [118]. One layer is the flow layer, where the fluid of interest is guided through microchannels. The other layer is the control layer, where the microchannels contain air or fluid and can selectively modulate the liquid in the flow layer. Each layer is fabricated on separate master moulds, and PDMS can be cast or spin-coated to the desired thickness. The layers can then be aligned over one another, forming one composite PDMS device [19]. PDMS is the most commonly used material when it comes to microfluidic fabrication. It possesses many attractive qualities such as elasticity, biocompatibility, transparency to visible and UV light, controllable surface chemistry and the ability to irreversibly bind to different materials (itself, glass and silicon) [19], [118]. It also has weak surface energy, making it easy to peel off the master moulds [119].

3.2.2 Microvalves for sample manipulation

Various types of microvalves and pumps are used for precise sample manipulation. They are firstly categorized as either active or passive. From there, active valves can be mechanical (magnetic, electric, piezoelectric and thermal), nonmechanical (electrochemical, phase change and rheological) or external (modular and pneumatic) [120]. Similarly, passive valves can be further classified as mechanical (flap, membrane, ball and in-line mobile structure) or nonmechanical (diffuser and capillary) [121], [122]. Pneumatic, in-line on-chip microvalves were first reported by Quake's group [123]. Typically, they consist of two layers of PDMS microchannels aligned perpendicularly over one another. A pneumatic valve will deform when pressure is applied to the valve channel and block the fluid flow in the adjacent fluidic channel, partially or entirely, depending on the pressure applied (***Figure 3-2***).

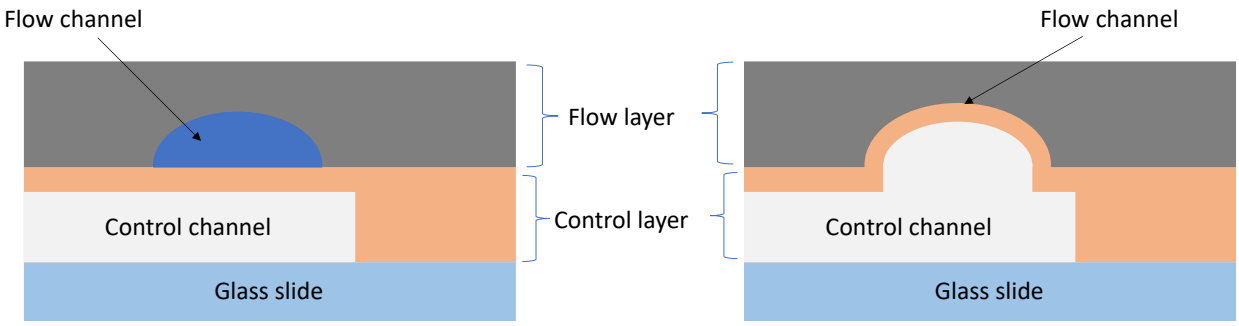

***Figure 3-2: Pneumatic microvalve schematic (not to scale)**. A control channel (valve) can pass underneath the flow channel. When pressure is applied, the valve compresses the separating membrane down, creating a seal in the flow channel.*

Some valves can be intentionally leaky, sieve valves, and they are useful for trapping beads, particles, cells or other analytes while still allowing fluid to pass [124]. Using this type of valve allows for chromatography techniques to be employed in LOC devices[125]. The microfluidic device discussed within this thesis used a sieve valve to trap microbeads, building a column on-chip (***Figure 3-3***).

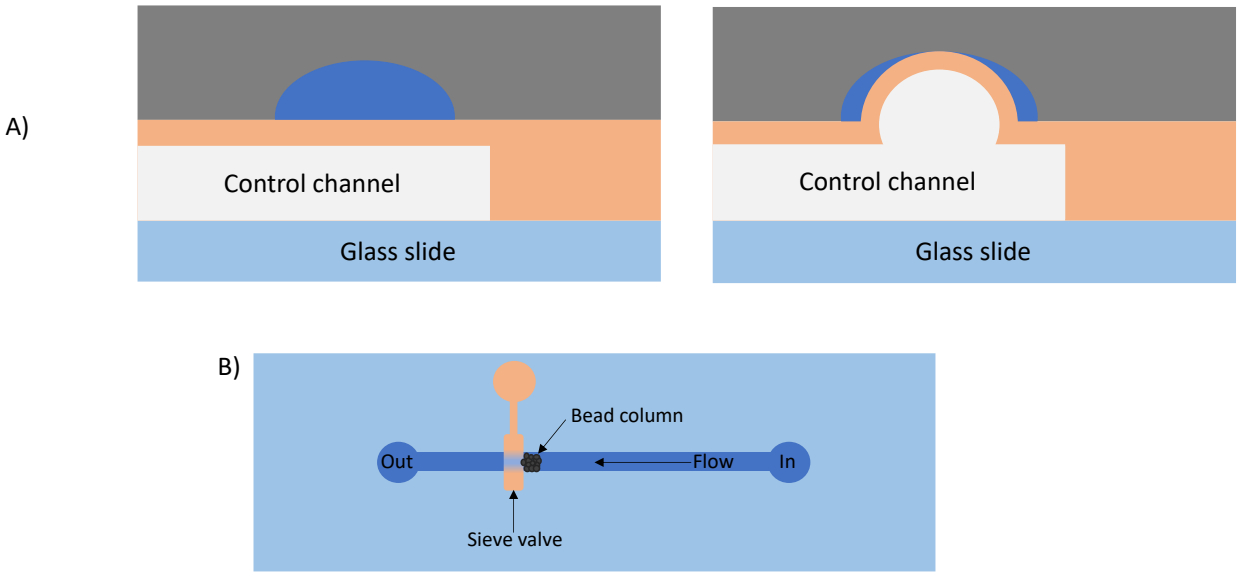

***Figure 3-3: Sieve valve schematic.** Trapping beads and forming a column on-chip while still allowing fluid to pass.*

Laminar flow is defined by fluid flowing in parallel lines with little to no mixing between adjacent lines. Flow within microfluidics is laminar due to the low Reynolds number [126]. Sufficient on-chip mixing has proven to be difficult because of laminar flow and usually relies on slow diffusive forces [126]. Pneumatic peristaltic pumps are a popular active pump system, often employed within microfluidic systems [121]–[123], [127]–[129]. This type of pump consists of at least three pneumatic valves that transport fluid by closing part of the channel synchronously (***Figure 3-4***) [123]. There are a few key advantages to using this type of pump system within a microfluidic platform. Firstly, it is capable of continuous-flow and fixed-volume mixing [130]. The second is this pump system can produce bi-directional flow rapidly. Lastly, sample contamination is minimized because the pump's external actuating components never contact the solution in the channel [123].

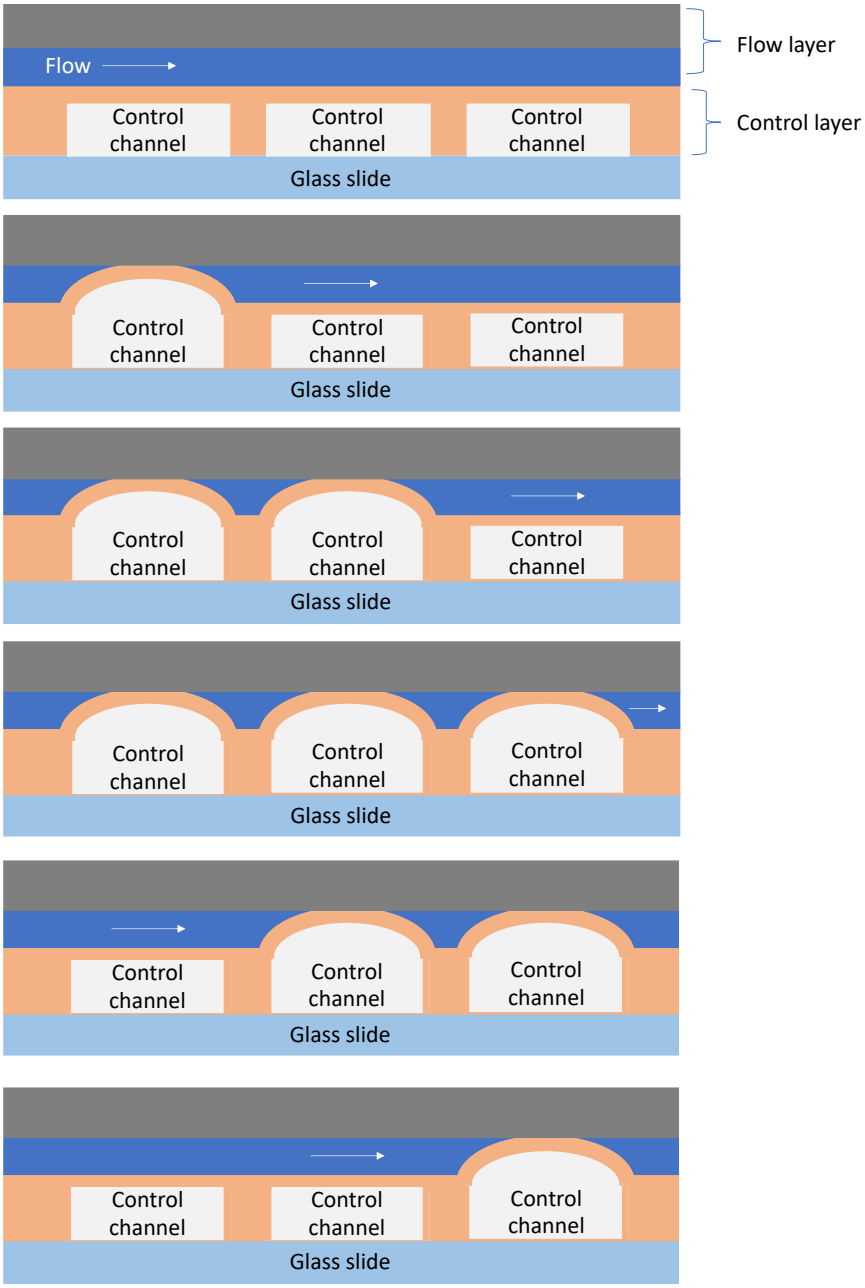

Figure 3-4: Peristaltic pump pattern schematic.

This chapter explores the design validation involved in the fabrication and experimental use of a preconcentrating microfluidic device. Determining the ideal membrane thickness for proper valve function and optimizing the peristaltic pump pattern sufficient flow in a fixed-volume were the significant milestones.

3.3 Experimental

3.3.1 Operational principle and design

The microfluidic channel architectures used in this thesis were designed in a CAD program (Clewin4©). The design was realized on a photomask, with either a positive or negative polarity, by CAD/Art Services. The photomask is later used during photolithography to transfer the design onto a photoresist coated silicon wafer. The microfluidic system consists of four major components: a peristaltic pump (***Figure 3-5 valves 5-7***), a sieve valve and a concentration loop (***Figure 3-5 C***) and a nanopore sensing region (***Figure 3-5 C***). The concentration loop holds a volume of 20 nL. The microfluidic device design consists of three PDMS layers (***Figure 3-5***) to incorporate a solid-state nanopore. However, because no nanopore was integrated into the devices used for validation, all devices in this thesis were made of two-channel layers. Two different device orientations were compared. The first validation device's (Device 1) top layer housed the control channel (valves) and the bottom layer was the fluid channel (***Figure 3-6 A***). The second validation device (Device 2) was oriented in the reverse order; the top layer was the fluid layer, and the bottom layer was the control (***Figure 3-6 B***). The device consisted of 9 open/close valves, one sieve valve and a 3-valve peristaltic pump for a total of 13 valves (***Figure 3-5 B***). The widest fluid flow channel sections (preconcentration loop) are 200 µm, and the narrowest (channels between valves 5-7 and valve 3) are 50 µm.

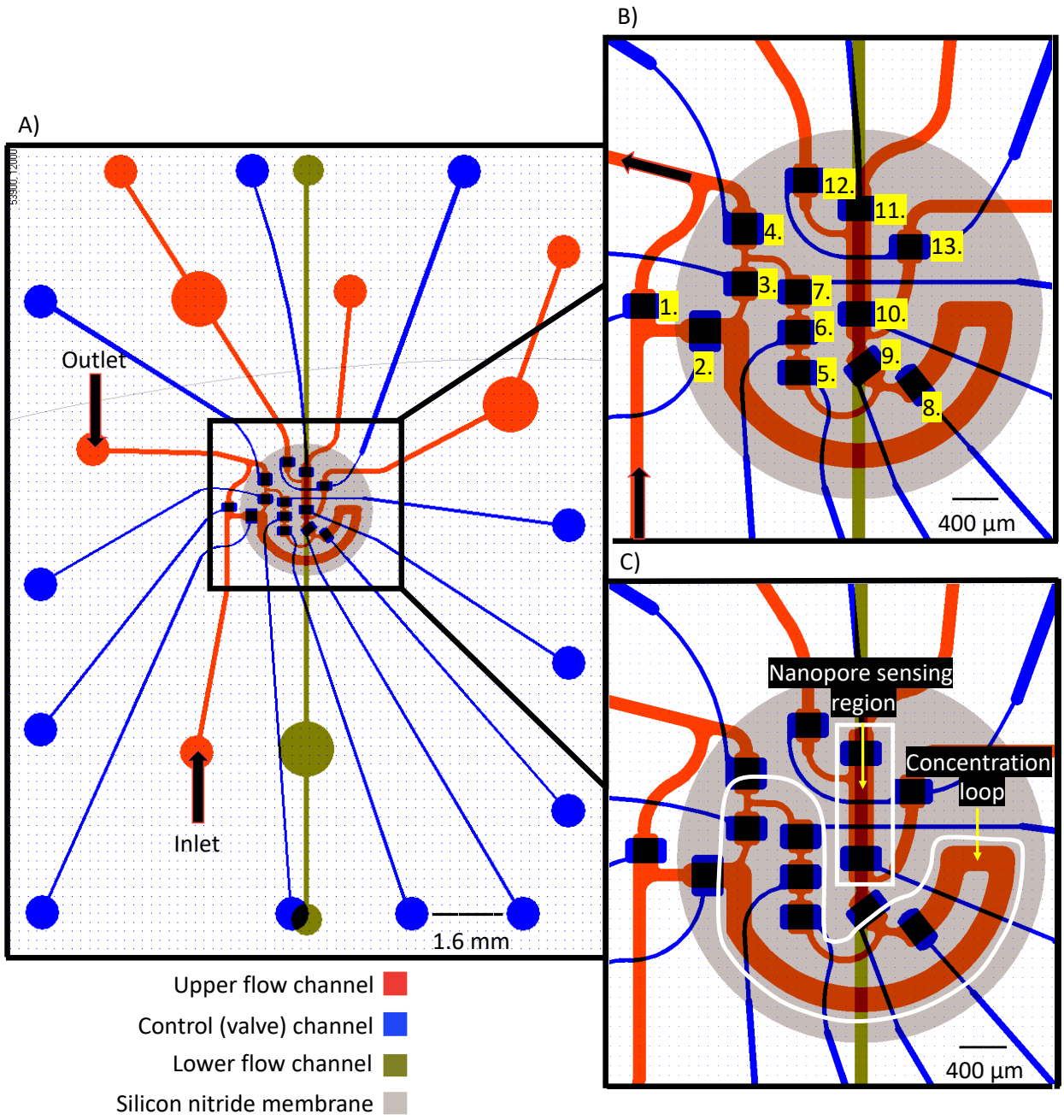

Figure 3-5:Clewin4 © image of preconcentrating microfluidic device. *A) The sample is introduced in the upper flow channel at the inlet. The blue control channels (valves) manipulate the same channel path in the upper flow channel. The silicon nitride membrane for nanopore fabrication is indicated in grey. Once the sample flows through the nanopore, it enters the lower flow channel and exits the device. B) Valves numbered 1-13. Valves 1-4 and 9-12 are open/close valves, valves 5-7 are peristaltic pumps, and valve 8 is a sieve valve. C) highlighting the concentration loop, where the sieve valve traps the beads and the nanopore sensing region where the nanopore will be fabricated.*

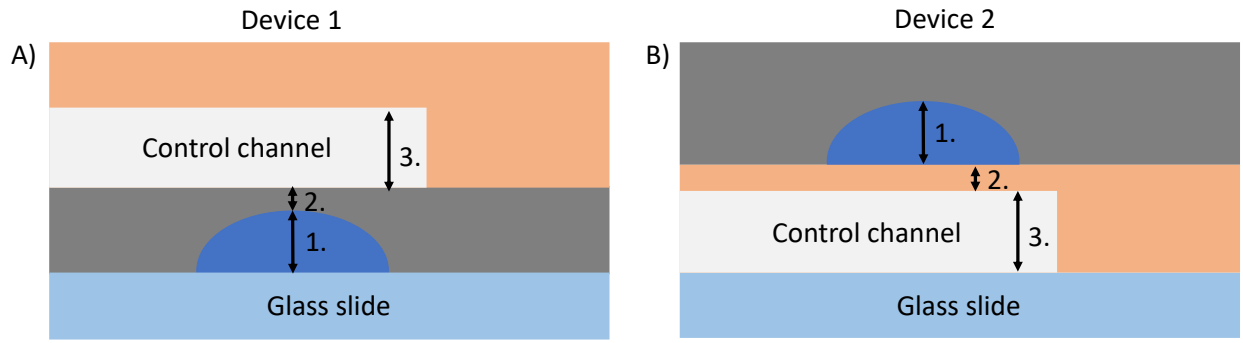

1. Fluid channel height: 20-25 µm
2. Membrane thickness between control channel and fluid channel: varied
3. Control channel height: 70 µm

Figure 3-6: Microfluidic layer orientation and specs for (A) Device 1 and (B) Device 2.

The sample is introduced at the inlet. By closing valves 1, 3, and 9, the fluid will travel around the loop and out of the outlet. Closing valves 2, 4 and 9 and opening valves 1 and 3 create a closed-loop system. The peristaltic pump (valves 5-7) flows the sample around the loop. This design also allows the sample to pass directly from the inlet to the outlet without being introduced to the concentration loop. Opening valve 9 allows fluid to flow towards the region dedicated to nanopore sensing. (***Figure 3-6***)

3.3.2 Microfabrication

Master moulds of each layer were fabricated using photolithography. Polished silicon wafers were cleaned using acetone, ethanol and isopropyl alcohol (IPA), in that order, and dried using an N_2 gas gun. Wafers were then plasma treated using oxygen plasma (AutoGlow Research) for 10 minutes at 200W and placed on a 200°C hot plate for 10 minutes. After cooling, approximately 1 mL of SU8-10 negative photoresist was added to the wafer and spin-coated (WS-400BZ-6NPP LITE spin coater) to achieve a 10 µm thick layer (***Table 3***). The wafer was then pre-baked, soft-baked and allowed to cool. Times and temperatures for all wafer baking are in ***Table 4***. Once cooled, the wafer was exposed to UV, with no photomask, using OAI Hybralign Series 200 mask aligner (UV intensity 15.3mW/cm$^{3)}$. This layer is a sacrificial layer that helps adhere to the next layer's features to the wafer [131]. The wafer was then post-baked, cooled and developed in SU8 developer (Kayakli Advanced Materials) for 2 minutes,

continually agitating. The wafer was rinsed and dried using the N_2 gun and hard-baked for 5 minutes at 150℃. For the fluid flow layer, around 1 mL of AZ-4620 was poured on the wafer and spun to 10 µm. The wafer was pre-baked, soft-baked and cooled. Then, another layer of AZ-4620 was poured onto the wafer and spun to achieve the desired final thickness of 20-25 µm. The wafer was pre-baked, soft-baked and then left to sit for three hours in a petri dish with a wet wipe to rehydrate. Exposure to UV was done using the fluid channel photomask in 10-second intervals to avoid cracking of the features. The wafer was developed for 5 minutes in AZ 400K developer 1:4; then, it was rinsed with diH_2O and blow-dried using the N_2 gun. The wafer was post-baked and hard-baked to allow reflow.

Table 3: Spin speeds for fluid flow wafer.

Layer	Spin speed
SU8-10 10 µm	1. 500 rpm* ACL*- 1995 10 seconds 2. 3000 rpm ACL- 1995 30 seconds 3. 0 rpm ACL-1995 10 seconds
AZ-4620 11.5 µm	1. 500 rpm ACL-100 10 seconds 2. 1600 rpm ACL-600 60 seconds 3. 500 rpm ACL -400 10 seconds 4. 1000rpm ACL -250

	10 seconds 5. 0 rmp ACL -200 10 seconds
AZ-4620 11.5 µm	1. 500 rpm ACL-100 10 seconds 2. 1600 rpm ACL-200 60 seconds 3. 500rpm ACL=200 10 seconds 4. 1500rpm ACL-250 10 seconds 5. 0 rpm ACL -200 10 seconds

*rpm= revolutions per minute
*ACL= acceleration

Table 4 Fluid flow wafer baking times and temperatures.

Layer	Pre-bake	Soft-bake	UV exposure	Post-bake	Hard bake
SU8-10	1 min- 65℃	5 min- 95℃	10 sec	1 min- 65℃ 2 min- 95℃	5 min- 150℃
AZ-4620	30 sec- 75℃	1 min, 25 sec- 110℃	None	None	None
AZ-4620	30 sec- 75℃	2 min, 45 sec- 110℃	60 seconds (10-second intervals)	2 min- 65℃ 2 min- 95℃	4 min- 120℃ (reflow)

The same wafer preparation steps mentioned above were performed for the control channel layer, along with the sacrificial layer of 10 µm SU8-10. After post-baking the sacrificial layer, the wafer was allowed to cool. Approximately 4 mL of SU8-50 was poured off the wafer and spun to the desired thickness of 70 µm (***Table 5***). The wafer was pre-baked, soft-baked and exposed to UV with the control channel photomask. All baking times and temperatures can be found in ***Table 6***. After exposure, the wafer was post-baked, cooled and developed for 6 minutes, 30 seconds. It was then rinsed with IPA, dried with the nitrogen gun and hard-baked. Following fabrication, all moulds were silanized using trichlorosilane (tridecafluoro-1, 1, 2, 2-tetrahydrooctyl, Sigma Aldrich) to promote the peeling of PDMS. The fluid flow final feature height was 20-25 µm, and the control channel's final feature height was 70 µm. A stylus profiler (DektakXT) was used to check the feature measurements.

Table 5: Spin speeds for control channel wafer.

Layer	Spin speed
SU8-10 10 µm	1. 500 rpm ACL-1995 10 seconds 2. 3000 rpm ACL-1995 30 seconds 3. 0 rpm ACL-1995 10 seconds
SU8-50 75 µm	1. 500 rpm ACL-100 10 seconds 2. 1600 rpm ACL-300 30 seconds 3. 0 rpm ACL-300 10 seconds

Table 6: Control channel wafer baking times and temperatures.

Layer	Pre-bake	Soft-bake	UV exposure	Post-bake	Hard bake
SU8-10	1 min- 65℃	5 min- 95℃	10 sec	1 min- 65℃ 2 min- 95℃	5 min- 150℃
SU8-50	2 min- 65℃	9 min- 95℃	12 sec	2 min- 65℃ 7 min- 95℃	15 min- 150℃

All replicates were made by soft lithography using PDMS (Sylgard 184 elastomer kit) at a ratio of 10:1 base to curing agent (***Figure 3-7***). For moulds whose PDMS thickness does not require the utmost precision, the PDMS was mixed, poured on the mould and degassed for about an hour before curing in the over for (70℃) for an hour. For moulds whose PDMS thickness needed to be thin and precise, the PDMS was mixed, degassed for an hour, poured on a mould and spin-coated at the required speed to achieve the desired thickness (***Table 7***). The PDMS thickness between the control channel layer and the fluid channel layer was varied to determine the optimum thickness for ultimate valve closure. This is discussed in more detail in Section 3.3.4 Measurement of valve responses, but varying spin protocols are listed in ***Table 7***.

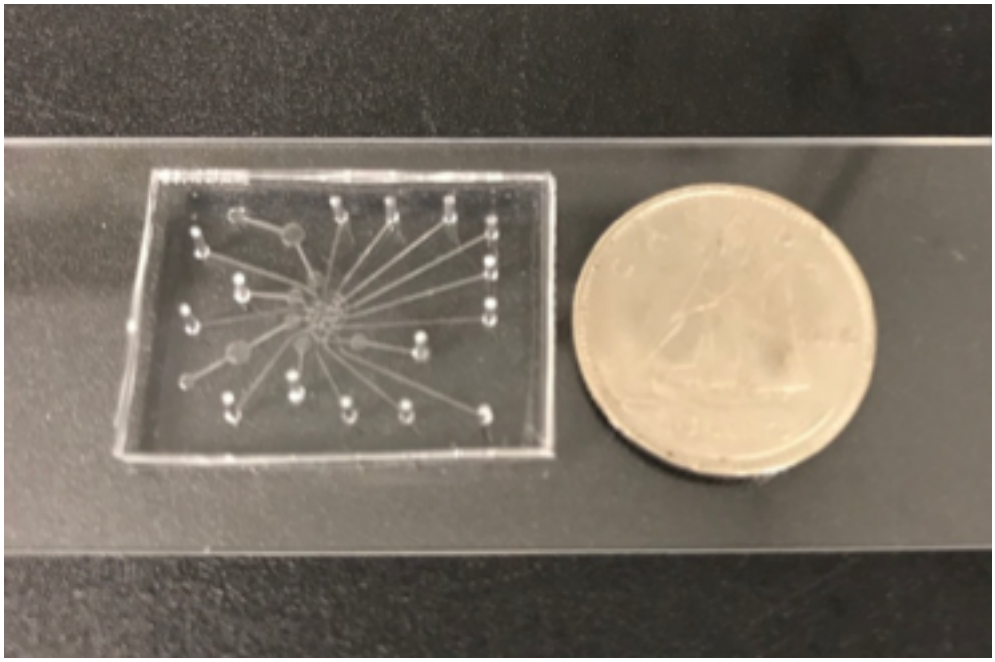

Figure 3-7: Photo of PDMS microfluidic device bonded to a glass slide. *A dime is placed beside the device for size reference.*

Table 7: Microfluidic device PDMS spin-coating protocols.

Device number and layer	Desired PDMS thickness	Spin-coating speed or PDMS poured
Device 1: fluid layer	30 µm	10 g of PDMS base, 1 g of PDMS curing agent mixed and spin-coated on wafer: 1. 500 rpm 1995 ACL 10 seconds 2. 2750 rpm 1995 ACL 30 seconds 3. 0 rpm 1995 ACL 5 seconds
Device 1: fluid layer	35 µm	10 g of PDMS base, 1 g of PDMS curing agent mixed and spin-coated on wafer:

		1. 500 rpm 1995 ACL 10 seconds 2. 2250 rpm 1995 ACL 30 seconds 3. 0 rpm 1995 ACL 5 seconds
Device 1: fluid layer	40 µm	10 g of PDMS base, 1 g of PDMS curing agent mixed and spin-coated on wafer: 1. 500rpm 1995 ACL 10 seconds 2. 2000rpm 1995 ACL 30 seconds 3. 0rpm 1995 ACL 5 seconds
Device 1: control layer	500 mm	25 g of PDMS base, 2.5g of PDMS curing agent, mixed and poured in the wafer.
Device 2: fluid layer	500 mm	25 g of PDMS base, 2.5g of PDMS curing agent, mixed and poured in the wafer.
Device 2: control layer	83 µm	10 g of PDMS base, 1 g of PDMS curing agent mixed and spin-coated on wafer: 1. 500 rpm 1995 ACL 10 seconds 2. 1000 rpm 1995 ACL 24 seconds

		3. 0 rpm 1995 ACL 5 seconds

3.3.3 Fluid flow set-up

To fill the control channel valves with ease, the microfluidic device is submerged in a water beaker and placed under vacuum for 30 minutes. This ensures all valves are full of liquid for optimal valve closure. Pressure-driven flow is used to introduce aqueous solutions to the microfluidic channels. Vials containing solution were connected to the device by polyethylene tubing. The components of the fluid-flow set-up used in this work are shown in ***Figure 3-8***. The flow was established by pressure regulators (BelloFram Corp Type-10 and SMC Precision Regulator IR100, IR 1010) connected to compressed air. The regulators supplied pressure to the vials through solenoid valves (The Lee Company, LHDA1223111H) that were on/off switches for the device valves. The solenoid valves were controlled by a custom-designed LabView software (National Instruments), DAQ (data acquisition) card (National Instruments USB-6001) and a DC Power Supply (Agilent E3630A).

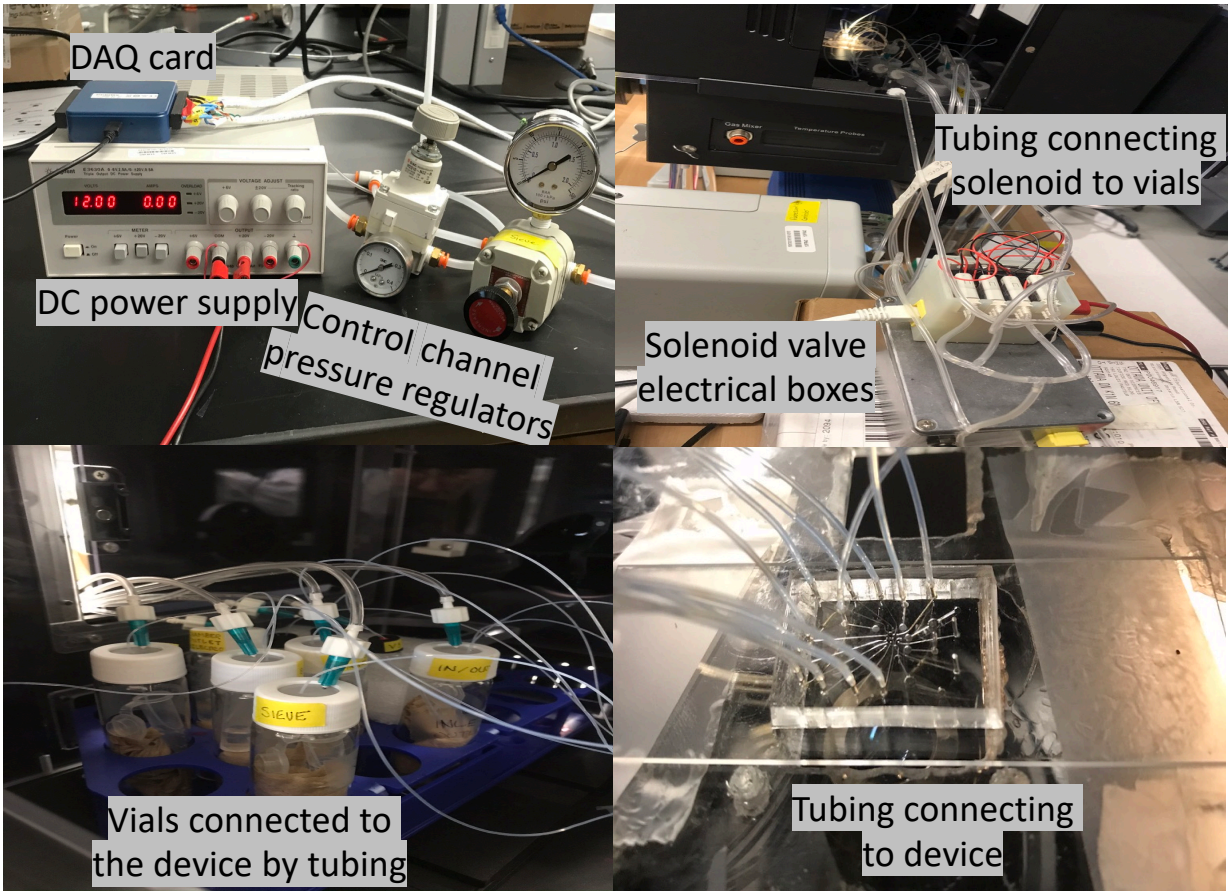

Figure 3-8: Fluid flow set-up. *The vials connected to solenoid valves and to the device were used to govern the control channel valves. When a valve was switched on using the LabView program, the solenoid valve would open, allowing compressed air flow to the vial. The fluid channel flow was controlled by pressure regulators connected directly to an inlet and outlet vial, containing the desired sample.*

3.3.4 Measurement of valve responses

Microvalve dynamics were monitored under an inverted optical microscope (Olympus IX51) equipped with a monochrome camera (Photometrics CoolSnap HQ 2). This microscope and camera set-up were used to monitor and capture all described device functions. To prepare for the experiments, food colouring was injected into the fluid flow channel to visualize valve closure better. diH_2O was used to fill the control channels. The device was submerged in diH_2O and placed under a vacuum for 30 minutes. In this work, membrane thickness between the control channel and the fluid channel and the orientation of the control and fluid layers (Device 1 vs Device 2 (***Figure 3-6***) were investigated to achieve optimum valve response. Membrane thickness for Device 1 and Device 2 varied from ~5 µm - ~15 µm.

3.3.5 Evaluation of peristaltic pump flow rate

Varying patterns and frequencies were investigated to determine the optimum flow rate. Three different methods were used and compared to track the flow rate from the peristaltic pump. The first method was collecting and weighing the amount of water displaced over an hour. Both pressure regulators for the inlet and outlet of the fluid channel were set equal at 7psi. The chosen pattern and frequency were set and carried out by the LabView program. Four centrifuge tubes were filled with water. Two centrifuge tubes were placed in each vial (inlet and outlet), one was attached to the polyethylene tubing, and the other was used to account for evaporation over the hour. Weight measurements for all four tubes were measured and recorded before and after the hour of peristaltic pumping using Sartorius AC121S analytical balance. The weight difference was converted to volume using water density and divided by the elapsed time (60 minutes).

The second method tracked the movement of an air bubble around the closed-loop. The fluid device channels were full of diH2O, and very carefully, a small (5 nL) air bubble was introduced to the loop. Again, valves 2 and 4 were closed to create a closed-loop. The camera was used to track the air bubble's movement and size over a period of time to determine the flow rate and ensure the bubble size remained consistent. The last method investigated tracked the movement of an oil bubble around the closed-loop. The protocol was the same as mentioned for the air bubble, except mineral oil (Lot #MKCF5662 Sigma-Alrich) was used to avoid gas compression. The volume of the loop and the time it took for the bubble to complete one full circle was used to calculate the flow rate.

3.4 Results & Discussion

3.4.1 Device layer orientation

Two device layer orientations were investigated: the control channel above the fluid channel (Device 1) or the control channel below the fluid channel (Device 2). Device 1 would allow for simpler nanopore incorporation because of how the layers are oriented. The nanopore needs to have access to the channel layer, and in Device 1, the nanopore could be

incorporated directly below the channel layer (replacing the glass slide). To incorporate a nanopore into Device 2, there would have to be access through the channel layer's PDMS.

Unfortunately, because of the complex mechanisms behind reflow (discussed later in this section), valves 3, 5, 6, and 7 did not fully close. All valves, excluding 3, 5, 6, and 7, closed under 20 psi. Even at a pressure of 60 psi, valves 3, 5, 6, and 7 did not close fully (***Figure 3-9***). The image of valve 3 at 20 psi and 60 psi shows an oval shape created by the valve layer touching down on the channel layer. The oval shape does not spread from one side of the channel to the other, as it does in the image of valve 10 at 20 psi, revealing the valve does not close fully.

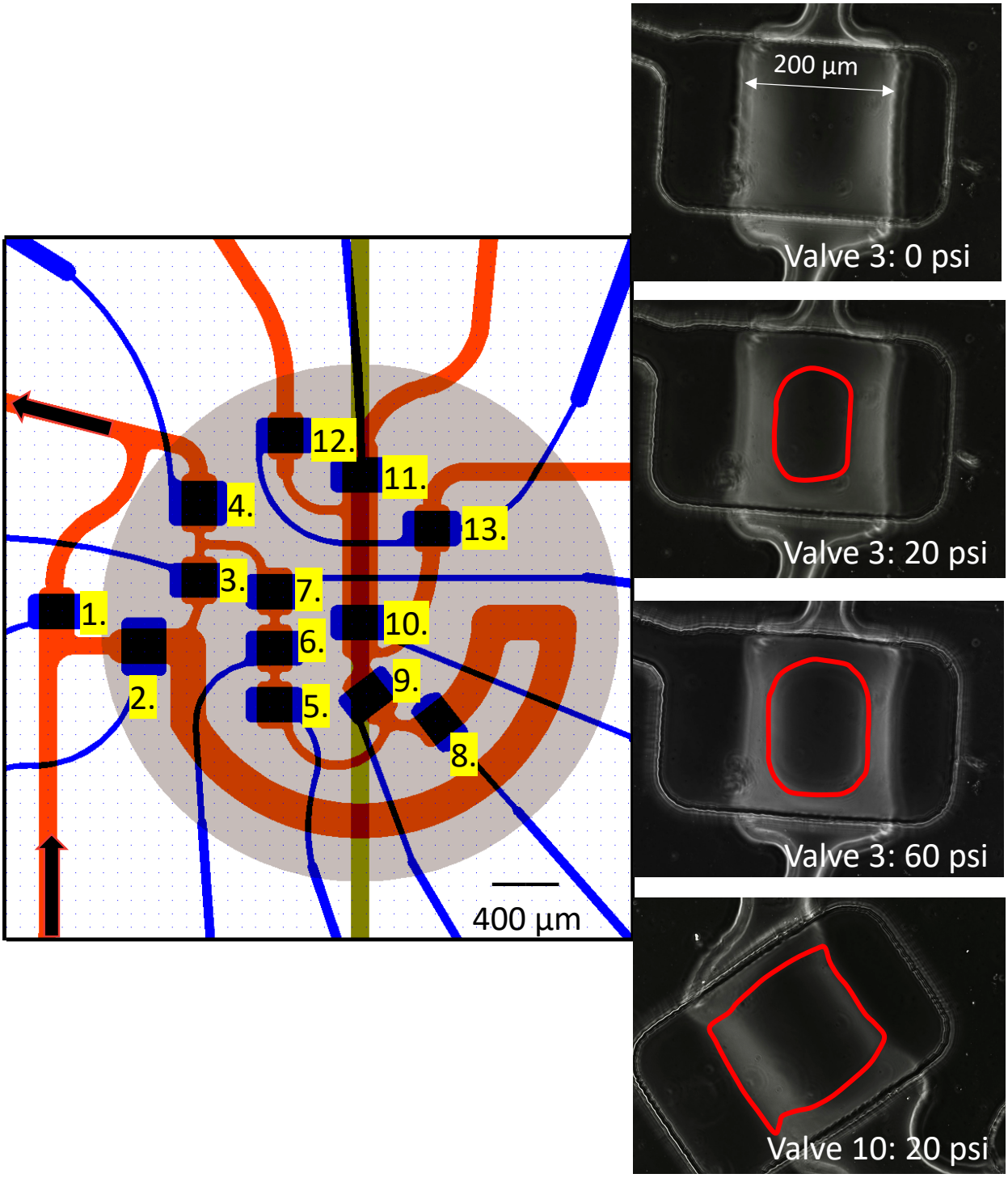

Figure 3-9: Device 1 valve closure. *Microscopic images on the right reveal incomplete valve closure; even at high pressures (60 psi), however, valve 10 achieves a full seal at 20 psi.*

The leaky valves became tremendously evident when attempting to build the microbead column in the preconcentration loop. More beads piled at valve 3 instead of valve 8, ultimately clogging the device before any useful experiments could be performed (***Figure 3-10***)

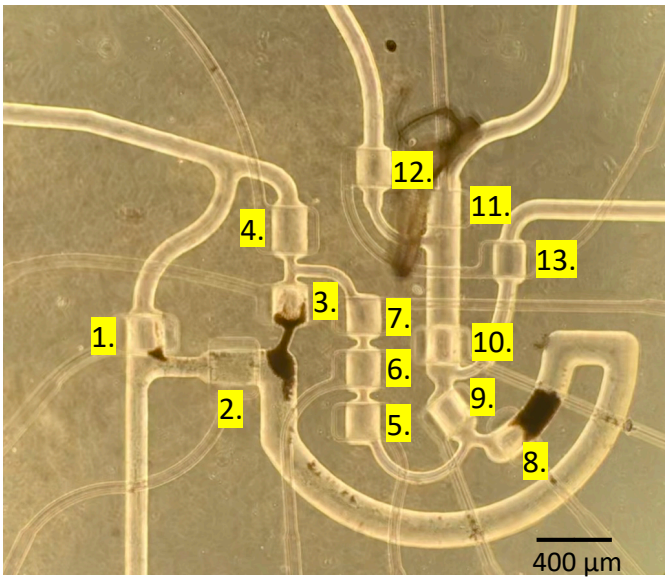

Figure 3-10: Introducing microbeads to Device 1: *beads group at valve 3, unintentionally, because of a leaky valve.*

As indicated in Section 3.3.2 Microfabrication different membrane thicknesses were investigated. First, the PDMS for the fluid channel layer was spun to a thickness of 35 µm. At this thickness, some valves did not close fully, as depicted in the above figures. If a membrane is too thick, it can restrict valve closure. When the PDMS for the fluid channel layer was spun to a thickness of 30 µm, the control channels started bursting into the fluid channels, indicating the membrane was now too thin. Fluid channel layer PDMS thickness was also tested at 40 µm. At this thickness, valves 3, 5-7 still did not close. Furthermore, valves that used to close, valve 1 and 9 notably, no longer sealed.

Measurements from a DektakXT profiler (0.5 nm vertical resolution) revealed a discrepancy in channel height (***Table 8***). The valves that did not close fully had channel heights > 30 µm. The optimum aspect ratio in the fluid channel for successful push-down valve closure should be 1:10 [132]. The width of the fluid channel where valve closure is desired is 200 µm, and the anticipated channel height from photolithography is ~20 µm, yielding the optimum

1:10 height: width ratio. All valves that have successful closure are around the 1:10 ratio; the valves that do not close fully (Valve 3, 5-7) have an aspect ratio of 1: 5 in some cases. Further investigation into the variance in fluid channel height leads to the physics behind the reflow process. The fluid channel wafer undergoes reflow to achieve rounded instead of squared channels. However, it has been noted that photoresist height can change in a complicated way during reflow because of differing design geometries [133]. All four valves that do not close fully have differing geometry; narrow channel widths merge into wide channel widths for valve closure. The process of reflow must alter the channel heights in those regions. The reasoning behind this is not clear and would require further investigation. One solution to this would be to remake the photomask so that all the channel widths are the same. However, this is not ideal because it increases the concentration loop's volume, reducing the concentration factor.

Table 8 Profilometer measurements for the fluid channel in valve closure regions ** bolded indicate valves that did not close fully **

Valve region number (from Figure 3-9: **Device 1 valve closure.**	Profilometer measurement (μm)
1	26
2	24
3	**40**
4	24
5	**35**
6	**35**
7	**37**
8	24
9	22
10	25

Another proposed solution was changing the orientation of the device. Analyzing the valve closure mechanism highlights how changing the top and bottom layers should allow for successful valve closure (***Figure 3-11***).

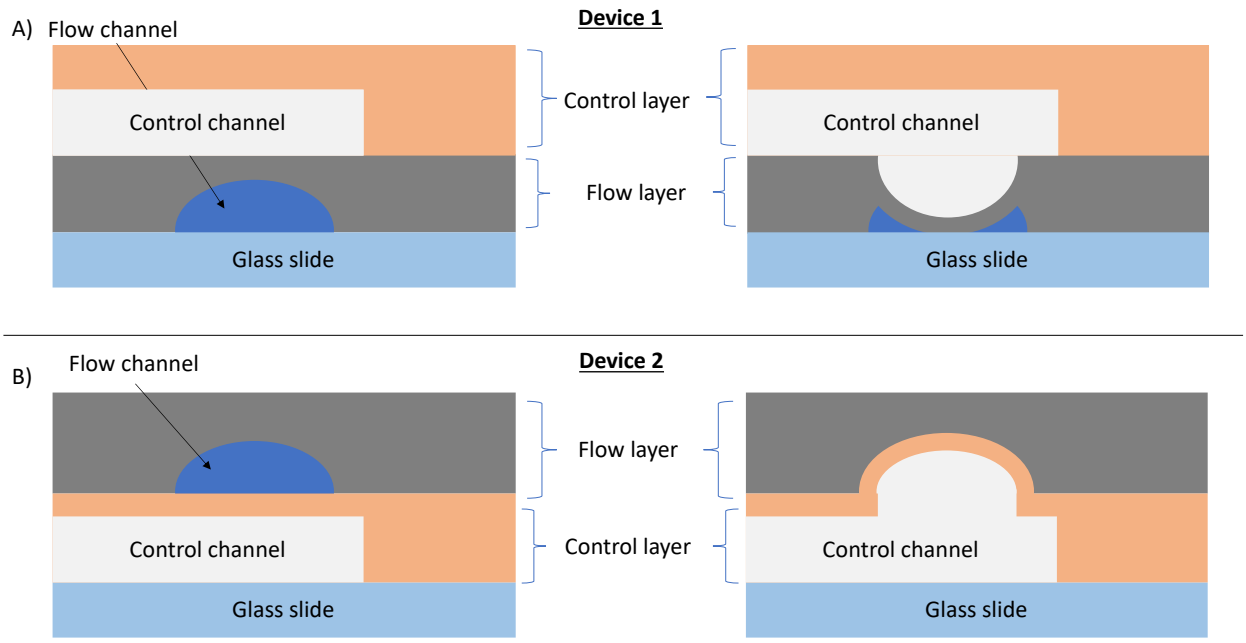

Figure 3-11: Analyzing valve closure under different device orientations. **not to scale* A) Device 1 valve may not close fully because of the control channel's geometry pushing down. B) Device 2 geometries are more favourable for complete valve closure.*

Changing the layer orientation to Device 2 allowed for all the valves to close completely (***Figure 3-12***), without designing and ordering a new photomask or compromising volume reduction. Device 2 makes for more complicated nanopore incorporation because it would have to be integrated above the fluid channel layer, and fluid access would need to be created through the PDMS of the flow channel layer. The use of different valves or different device designs should be investigated. All experiments from this point on are done with Device 2 to have complete valve closure.

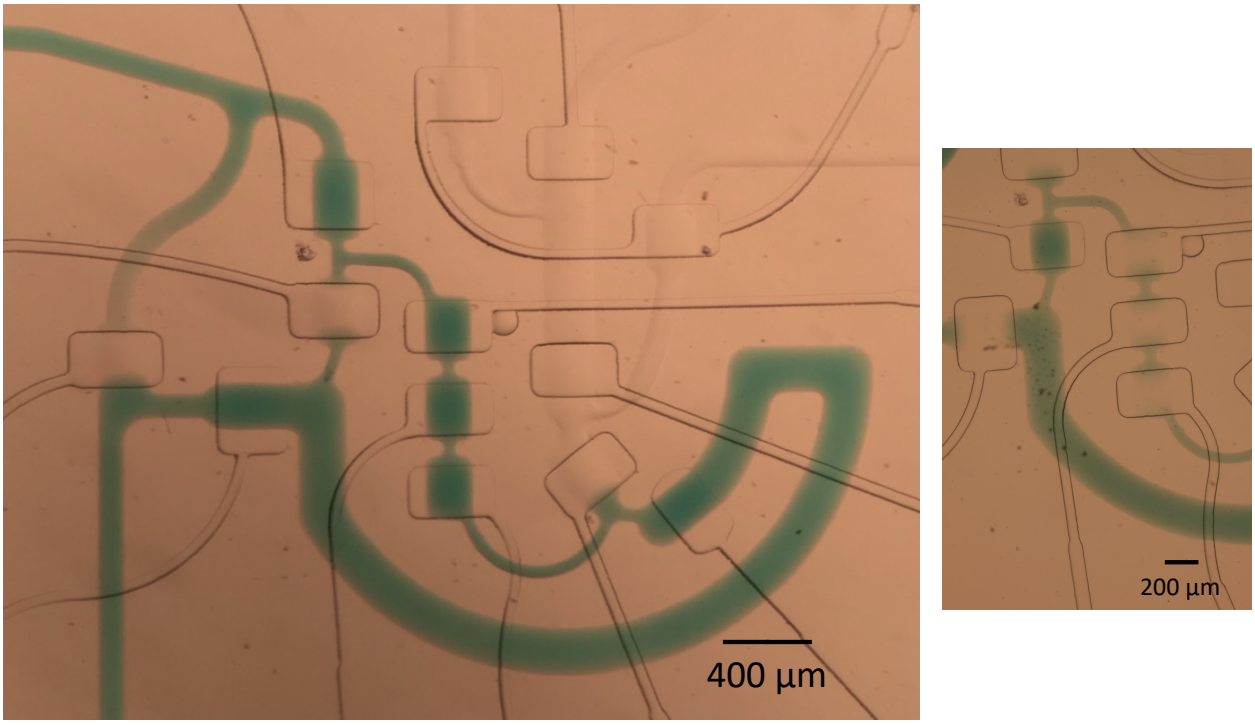

Figure 3-12: Device 2 valve closure: *after changing the layer orientation, all valves are completely closed.*

3.4.2 Pumping rate and pattern

The peristaltic pump flow rates for Patterns 1, 2 and 3 (***Table 9***) are compared in ***Figure 3-13***. The patterns were chosen from previous literature on peristaltic pumps; Pattern 1, 2 and 3 [122], [123], [128]. Pattern 1 had the highest flow rate for both measurement methods, followed by Pattern 2 and then Pattern 3. The flow rates obtained from measuring the displacement of water and tracking the air bubble are agreeable. Pattern 1 flow rates were 55 nL/min and 45 nL/min for water displacement and air bubble tracking, respectively. Pattern 2 flow rates were 31 nL/min and 32 nL/min for water displacement and air bubble tracking, respectively. Pattern 3 flow rates were 25 nL/min and 28 nL/min for water displacement and air bubble tracking, respectively. Flow rates were measured on three different devices, and all measurements were quite similar from device to device, indicated by the small standard deviation error bars.

Table 9: Peristaltic pump patterns

Pattern number	Pattern
1	100 110 010 011 001
2	100 110 111 011 001
3	100 110 111 011 001 101

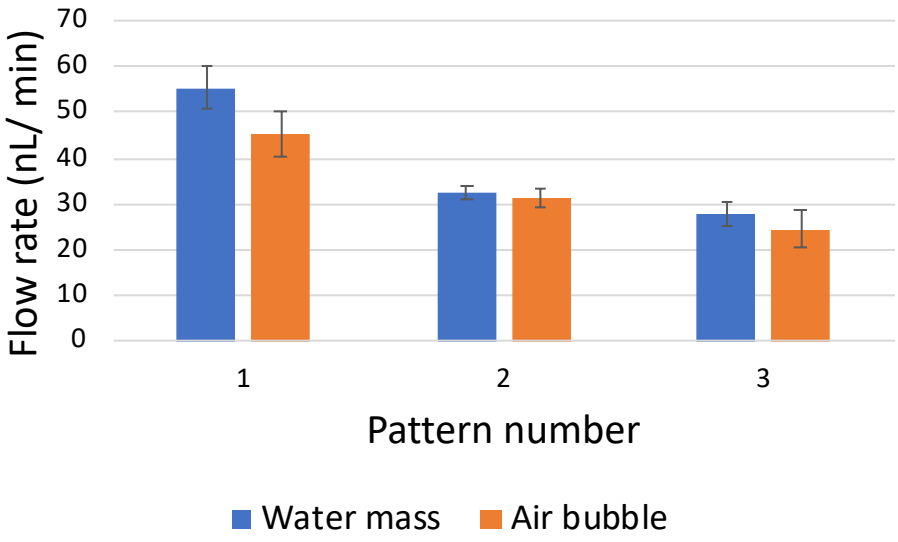

Figure 3-13: Flow rates for different pumping patterns. *Pumping patterns were gathered from 3 devices and were taken in replicates of 3. All measurements were performed at 68.5 cycles/min.*

The effect of frequency and flow rate were also compared for Pattern 1, as results indicate it provided the best flow rate in this device. Cycles per minute were increased, and the flow rate was monitored through air bubble tracking (***Figure 3-14***). This flow rate determination method was used because it is similar to that of displaced water; however, it is much more time-efficient. An optimum flow rate of 48 nL/min was achieved when the pattern operated 100 cycles per minute. When the pump was run at a higher frequency, the flow rate started to decline. Using the same pattern, Xiang *et al.* achieved a maximum flow rate of 274 µL/min, at a driving speed of 170 cpm [123]. The channel they were testing was much larger than the device being investigated in this thesis; Xiang *et al.* had a cross-sectional area of 67500 μm^2 versus 4000 μm^2 is the largest cross-sectional area in the 20 nL concentration loop for the device in this thesis.

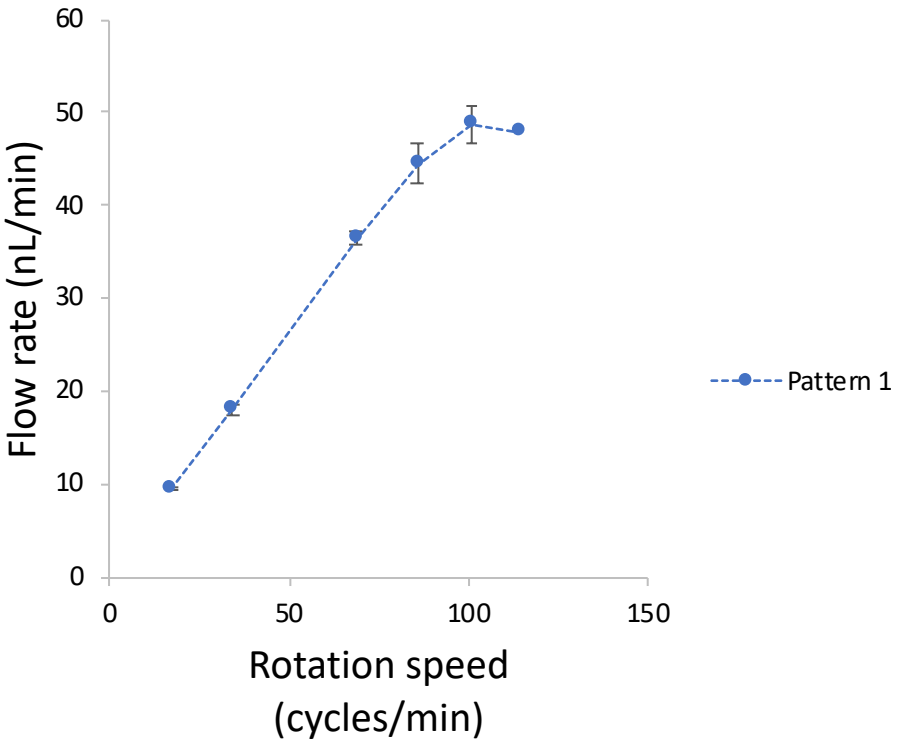

Figure 3-14: Effect of pump pattern frequency on flow rate. *The flow rate increased steadily with rotation speed until an optimum flow rate was achieved around 100 cycles per minute; above that, the flow rate started to decline.*

It remains a challenge to try and quantify the flow rate within a microfluidic device. The method of measuring displaced water is perhaps the most accurate; however, it is very time-consuming when comparing multiple patterns, multiple frequencies and multiple devices. Given the time frame, it was not practical to determine optimal frequency using this method. Tracking an air bubble around the loop is much more time-efficient and reasonably agreeable to water displacement measurements. However, the air bubble can expand and compress, which can cause inaccuracies in the results. An oil/water interface was also tried to monitor the flow rate, as oil would not compress like air. However, every time the oil bubble passed through the peristaltic pump, it would break up into many little bubbles, so this method was retired. Even though hard to characterize precisely, the flow was still achieved within a closed-loop system, on-chip using a peristaltic pump. The effect of the mixing of the peristaltic pump is investigated in Chapter 4 through monitoring on-chip elution of DNA.

3.5 Conclusions

This chapter focused on several validation experiments for the preconcentrating microfluidic device. The first hurdle was to troubleshoot valve closure; without proper valve closure, the device would be null. If time were not a constraint, perhaps a different device design could be optimized to reduce issues of raised channel height caused by reflow. Feasibly if the channels gradually got larger or smaller, the channel height increase would not be so prominent, which could be a long-term solution. Nonetheless, changing the device orientation from Device 1 to Device 2 solved the valve closure problem.

The next step in device validation was determining the best peristaltic pump pattern and frequency to facilitate elution on-chip. Accurate evaluation of flow-rate remains a challenge for this system; however, an optimum flow was achieved by Pattern 1 at a speed of 100 cycles per minute. After successful validation, the device is now ready for the ultimate test: increasing sample concentration on-chip.

Chapter 4 : Incorporating Microbead Assays with a Microfluidic Device

4.1 Motivation and Objectives

Microfluidics is an exciting and developing field that has the potential to solve many analytical challenges. These systems can perform a vast range of traditional lab protocols, including sample pre-treatment, transport, mixing, separation and detection. Researchers have reported performing sample preparation processes, like preconcentration, purification and labelling, all on a microfluidic platform. The incorporation of micro-tools (microvalves, micropumps, microfilters and micro-detectors) within a microfluidic device has made all these processes possible. These micro-tools, combined with well-developed microbead assays, present an opportunity to address sensitivity issues with solid-state nanopore sensors. This stage of the project combined efforts in Chapter 2 and Chapter 3 to perform sample concentration on-chip.

4.2 Introduction

Microfluidic systems have been used to preconcentrate and purify solutions, which are exciting steps towards improving detection, especially for low concentration targets in complex samples [134]. Superior concentration and purification can be achieved using microfluidics because of the extreme volume reduction and precise fluid manipulation that are not possible using traditional benchtop methods [135]. There are two popular methods for sample preconcentration; using electro-kinetics and through surface binding. Electrokinetic strategies have successfully increased concentration within microfluidic devices [136], [137]; however, most biological samples are complex and require more specificity for single target isolation.

Surface binding techniques are another popular method for preconcentration that can offer specificity through surface modifications [138]. These techniques adsorb or bind analytes onto monolithic materials or microbeads, trapping all the targets in a confined space. This entrapment allows for sample concentration and sample purification once the target is isolated [57], [139]. Typically, trapping analytes by a monolithic material involves flowing the sample to the monolith and separating analytes by hydrophobic interactions [138]. Monolithic materials

can be scaled down for successful incorporation within microfluidic platforms [140]–[142]. Using microbeads for sample concentration within microfluidics is another feasible method that exploits surface binding interactions. With the advances made concerning microtools, beads can be trapped using on-chip filters [143], sieve valves [144] or magnets if magnetic microbeads are used [139]. Many targets could be purified and concentrated using one microfluidic device because many different types of microbead assays are commercially available. Though this thesis specifically investigates a DNA microbead assay within a microfluidic device, one could imagine selecting the bead assay that suits the desired target and introducing the beads and sample to the microfluidic device for purification and concentration. Based on the DNA capture results from Chapter 2 and the volume reduction by the device in Chapter 3, a concentration increase of 100X is expected.

Fluorescence intensity is one of the most common methods used to monitor LOC systems because of its high sensitivity and readily available fluorophores [145]. It can be used when the sample is confined within a device made from PDMS, a popular material for LOC fabrication [146]. Though this technique is widely used, it still suffers from certain drawbacks because of the sensitivity of fluorescent dyes. The dyes are often costly, have a short shelf life, and are reactive to their environment (pH, temperature) [145]. Furthermore, photobleaching remains an issue when using fluorescence microscopy and limits the reliability of results when this method is used. Photobleaching irreversibly destroys fluorophores, ruining fluorescent measurements [147]. Fluorescence measurements are initially used to monitor on-chip concentration; however, the end goal is to use solid-state nanopores to avoid all the complications involved with fluorescence microscopy.

4.3 Experimental

4.3.1. Microfluidic chip preparation

See Section 3.3.2 Microfabrication for information on how the device was assembled. Before starting an experiment, the microfluidic device was oxygen plasma (AutoGlow Research) treated at 30 watts for 30 seconds to make the channels hydrophilic. The device was

submerged in diH_2O and placed under vacuum for at least 30 minutes, thoroughly wetting and filling all channels. These steps were done for a couple of reasons; easier filling of the control channel valves and diminish microbeads aggregating. After attaching all of the tubings to the device, the fluid channel was flushed thoroughly with wash buffer to ensure no diH2O was left, as that could result in the elution of DNA from the beads.

4.3.2. Capture and isolation of target DNA using MagSi DNA 3.0 COOH

DNA fragments of 50 base pair (No limits, Thermofischer SM1421) were diluted to 10 ng/µL in 50 µL of diH2O and then mixed with 3 µL of MagSi DNA 3.0 COOH magnetic microbeads* in 111 µL of binding buffer (Section 2.3.1 Capture and isolation of target DNA using COOH coated magnetic beads). Once DNA was bound to the beads, the beads were washed twice in the wash buffer. After two washes, the beads were resuspended in 100 µL of wash buffer and ready to be introduced to the microfluidic device. The bead and wash buffer mix was vortexed if it sat for longer than 5 minutes before introducing the microfluidic device. Vortexing the mixture helped the beads stay in suspension longer, so there was less clogging when flowing the beads into the device. The protocol for bead elution is outlined in detail in ***Figure 4-1***. Air was introduced to the column to track buffer exchange because both the binding and elution buffer are clear, colourless liquids.

*Calculation for the volume of microbead solution can be found in the **Appendix**.

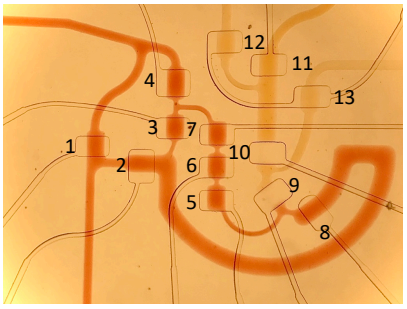

1. Preconcentration area of device is full of wash buffer (red), and ready for DNA coated microbeads. Valve 9 and 10 are closed to ensure no fluid goes to the nanopore region.

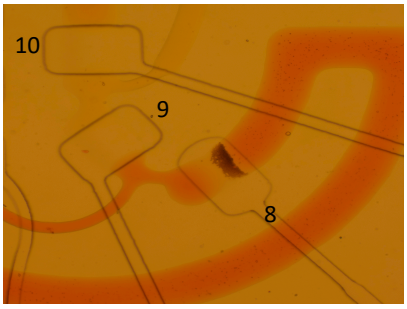

2. Valves 1 and 3 are closed so beads can flow around concentration loop. Valve 8 (sieve) is partially closed to capture beads

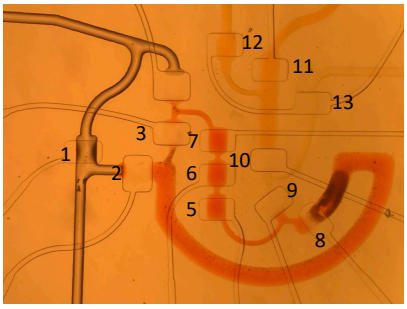

3. Once bead column is appropriate length* valves 2 and 4 are closed to create a closed-loop. Air is introduced to the bypass channel to remove the wash buffer bead sample.

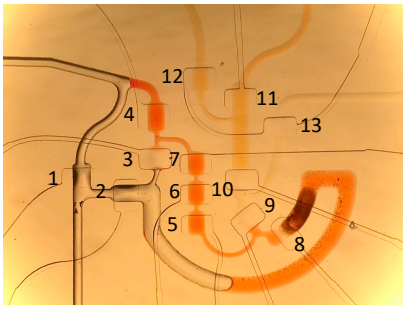

4. Air is slowly introduced to the rest of the device, after opening valve 2 and 4, to remove wash buffer and push all beads to the sieve valve before introducing the elution buffer.

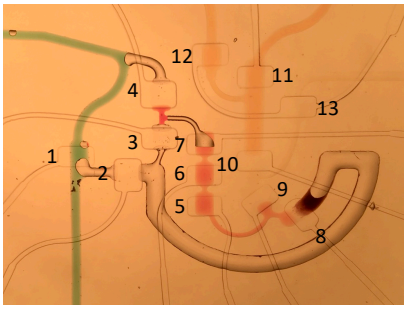

5. Air removes as much wash buffer as possible. Valve 2 and 4 are closed again and the elution buffer (blue) is introduced to the bypass channel.

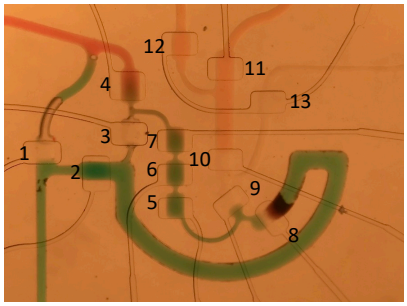

6. The elution buffer is slowly introduced to the concentration loop. Once it reaches valve 4, the device is switched to the closed loop (close valve 2 and 4)

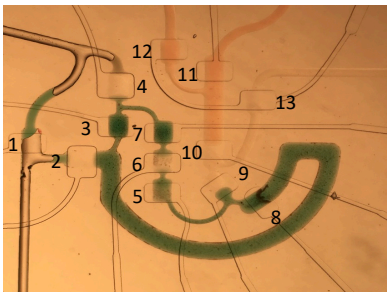

7. Valve 3 and 8 are opened to allow for a complete loop, and the peristaltic pump is activated to mix the beads with the elution buffer.

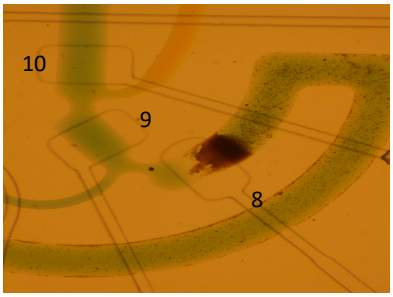

8. After sufficient mixing, valve 8 (sieve) can be closed again to recapture the beads. Valve 9 and 10 can be opened and the elution buffer can be sent to the nanopore sensor.

Figure 4-1: Elution on-chip protocol. *This schematic uses food colouring in place of buffers to highlight the buffer exchange and fluidic manipulations. *Not to scale* *Appropriate length for bead column: this requires some calculations and varies with the microbeads being used. See the appendix for more information. It should also be noted that even though magnetic microbeads were used, the microfluidic device had no magnet incorporated, the sieve valve strictly performed bead capture.*

Elution assays were monitored by fluorescence using an intercalating fluorescent dye, DAPI (4', 6-diamidino-2-phenylindole, ThermoFisher, D1306). Measurements and observations were performed using fluorescence microscopy under an X-Cite fluorescence lamp illuminator (Series 120 Q) and a DAPI filter. DAPI and diH_2O were mixed to achieve a final concentration of 1 µg/mL DAPI and introduced as the elution buffer. A side experiment was performed, same protocol outlined in Section 2.3.1 Capture and isolation of target DNA using COOH coated magnetic beads, except the elution buffer contained DAPI (1 µg/mL) to check for interference with DNA elution. The elution buffer was kept in a centrifuge tube, shielded from the light. The elution buffer was minimally exposed to light to reduce photobleaching effects. Elution progress was monitored over time, and images were taken at 150 ms exposure, 1X gain and 20X magnification. Pictures were captured over 10-second intervals at t= 0 (immediately after the elution buffer filled the preconcentration loop (***Figure 4-1 Step 6***); at t= 1 minute (one minute after peristaltic mixing) and t= 5 minutes (after five minutes of mixing). Peristaltic mixing of Pattern 1 was performed at the optimum speed of 100 cycles/min. When images were not being taken, the fluorescence light source was blocked by the shutter, and the device remained shielded from the light using a black box enclosure from Okolab (***Figure 4-2***).

Figure 4-2: Microscope set-up to monitor on-chip elution via fluorescence.

Fluorescent measurements (in relative fluorescent units, RFU) were compared against a standard curve of fluorescence for known DNA concentrations to give insight into the achieved concentration increase. 30 µL standard curve samples were made using Lambda DNA (New England Biolabs, N3011S) diluted in diH_2O to concentrations ranging from 500 ng/µL – 62.5 ng/µL. 10 µL of the sample was used to confirm sample concentration using the BioTek™ Epoch™. DAPI was mixed with the other 20 µL of the sample at a final concentration of 1 µg/mL. The fluorescence of these samples was monitored using the bypass channel in the microfluidic device. The camera focused on a specific spot in the channel under 20X magnification. Using Micro-Manager, images were taken over time to monitor the fluorescence for each sample. The images were analyzed using ImageJ to get RFU for each sample. A standard curve was made plotting RFU vs DNA concentration. On-chip elution protocol and measurements were performed immediately after standard curve measurements.

4.4 Results & Discussion

4.4.1. On-chip elution of DNA from MagSi COOH 3.0 beads

Images from the on-chip bead assay performed without DNA bound to beads and with DNA bound to beads are compared in ***Figure 4-3***. The blank experiment followed the same procedure, but no DNA was in the initial binding solution; hence no fluorescence signal appeared (***Figure 4-3 A***). When the protocol was performed with DNA attached to the microbeads, there was an immediate fluorescence signal that increased over time (***Figure 4-3 B***)

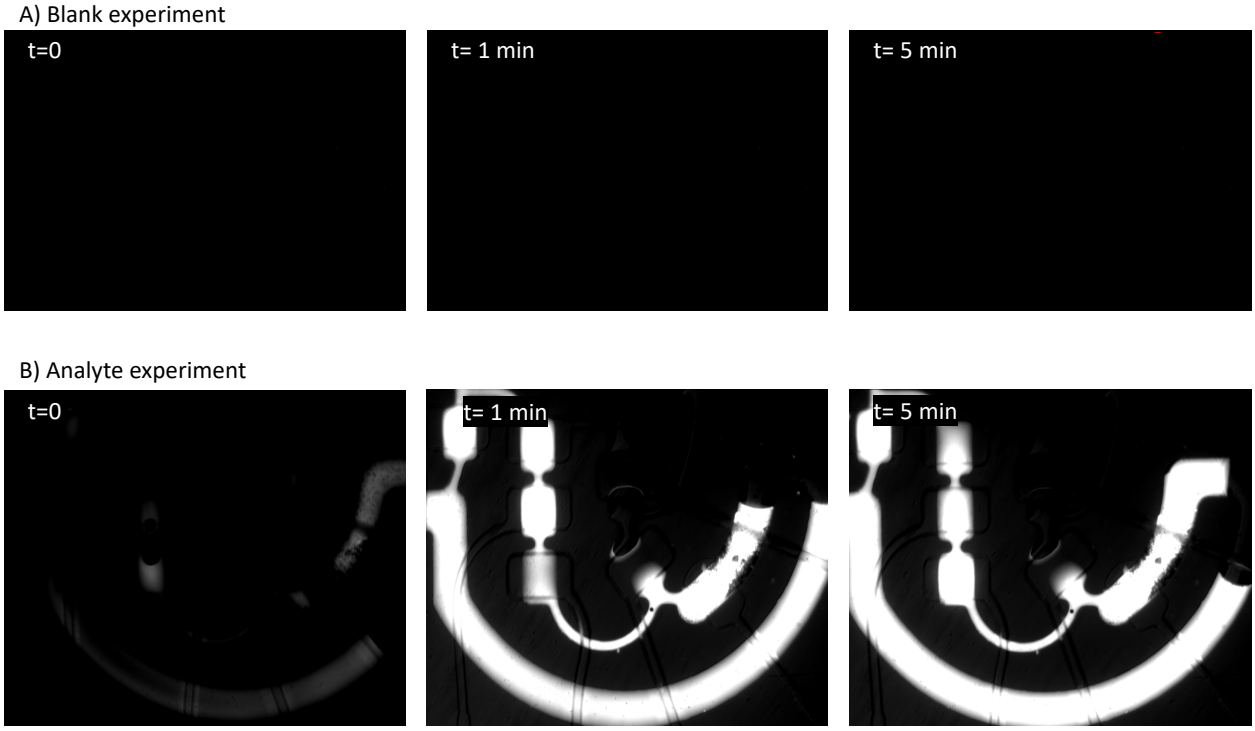

Figure 4-3: On-Chip elution of 50 base pair DNA from MagSi 3.0 COOH beads fluorescence images. *A) The experiment performed without DNA. B) The experiment performed with DNA. Images were taken at a 150ms exposure, 1X gain, 4X magnification. An air bubble is present in the part of the channel that shows no fluorescence.*

The fluorescence intensity remained constant, around 900 RFU, for the blank experiment. When DNA was attached to the beads, after one minute of mixing with the elution buffer, the fluorescence intensity increased to 2550 ± 90 RFU due to the release of DNA from the beads. After five minutes of mixing, the fluorescence intensity increased to 3850 ± 60 RFU.

Fluorescence was rechecked at ten minutes; however, the intensity had dropped significantly. This is likely due to photobleaching, which is an issue with fluorescent imaging. RFU for on-chip elution after one minute of mixing and after five minutes of mixing were compared to the standard curve to estimate on-chip concentration (***Figure 4-4***)

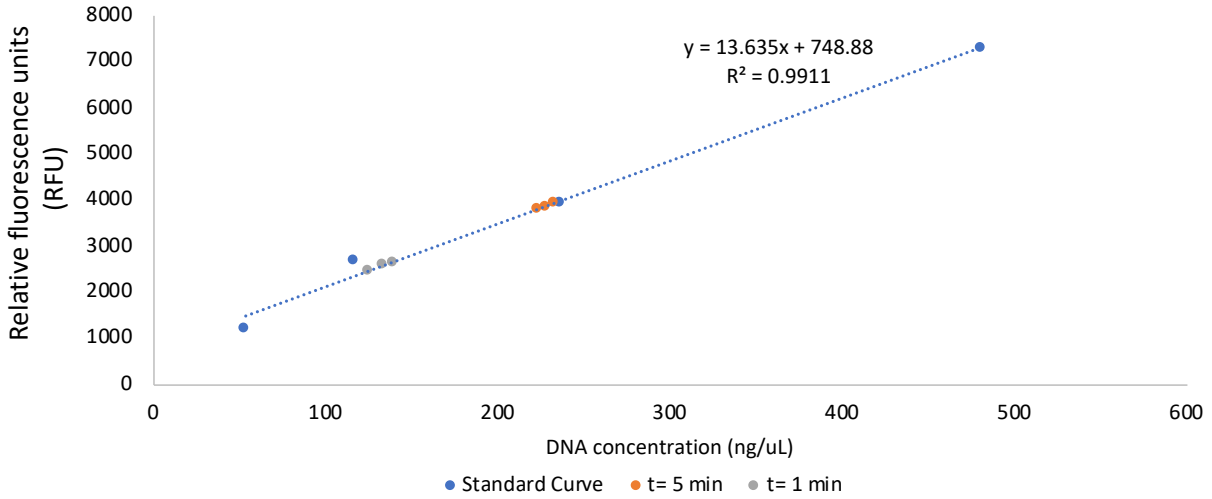

Figure 4-4: Relative Fluorescence Units for on-chip elution compared to the standard curve to determine DNA concentration. *Values for DNA concentration after 1 minute of mixing (grey) and after 5 minutes of mixing (orange)*

The estimated concentrations based on fluorescence were 132 ±7 ng/µL and 228 ±5 ng/µL after one and five minutes of mixing, respectively. The starting sample concentration, measured by BioTek™ Epoch™, was 8 ng/µL. The fluorescence measurements suggest that the concentration increase was 28.5 times. Based on calculations and experimental results in Chapter 2, the expected concentration increase was 100X (**Appendix**). It is possible that the concentration continually increased with pumping after the five-minute mark, and photobleaching may have distorted these results. Because the volume is so small on the microfluidic device, there is not another great method to validate the experiment. The ultimate test will incorporate a nanopore to determine if sensing time is decreased when combined with this method.

Another consideration is that the beads were 2X in excess of the recommended bead-to-DNA ratio for the amount of DNA in solution (**Appendix**). MagSi DNA 3.0 COOH beads can

bind ~15 µg of DNA per mg of beads. The initial solution contained about 500 ng of DNA, which would require 1.6 µL of bead solution. However, 3 µL of solution was used to increase the probability that all the DNA would be captured by a bead. Doubling the amount of bead solution means that not every bead will have DNA bound. This was not an issue in Chapter 2 results because most beads in the binding buffer were also in the elution buffer. It became a problem when the beads were introduced to the device, because not all of the beads could fit in the concentration loop. This led to half of the beads in the concentration loop not having DNA attached. This oversaturation of microbeads lowered the concentration factor; perhaps a 50X concentration increase would have been more accurate using this method (**Appendix**).

Much of the literature for on-chip surface binding techniques for DNA is targeted towards the purification of samples and not concentration increase. Reports for elution efficiency on-chip are between 70-80% [148], [149]. Both groups used similar sized silica particles (3-5 µm in diameter) packed within PDMS channels; however, the DNA they isolated were 600 base pairs [148] and 48 500 base pairs (lambda DNA) [149]. To achieve a higher on-chip elution efficiency, DNA fragments greater than 100 base pairs should be used. Increasing the elution efficiency would increase the concentration factor. Another option is to make a longer microbead column; however, this introduces prolonged flow rates. Short DNA fragments (< 100 base pairs) are not ideal for solid-state nanopore sensing, so if the desired sensing target is that small, it should be complexed with a larger structure [72].

4.5 Conclusions

The novel microfluidic device validated in Chapter 3 successfully captured microbeads on-chip utilizing a sieve valve. The peristaltic pumping system proved efficient at on-chip mixing, within a closed-loop, even with microbeads present. Fluorescence measurements suggest a concentration increase of 25X was achieved from the original DNA sample; the expected concentration increase was 100X. Issues of photobleaching and microbead saturation could be contributing to the lower than anticipated concentration factor. To achieve a higher concentration factor, a few things should be considered. Larger DNA fragments should be used to increase the elution efficiency. The number of microbeads should be lowered (1.25 or 1.5

times in excess), or a method for sorting microbeads with bound DNA from bare microbeads should be implemented in order to have all beads that are in the concentration loop have DNA bound. Nonetheless, this microfluidic shows promise for sample concentration.

Chapter 5 : Conclusions and Outlook

5.1 Summary and Accomplishments

The development of integrated microfluidic devices enables complex and sophisticated experiments to be performed on a single chip. These small devices are cost-effective to fabricate and operate, requiring small sample volumes. Another upside to these platforms is the ease of solid-state nanopore integration. Though no nanopores devices were used in this thesis, the results from sample concentration are promising for their later incorporation.

Chapter 3 reported a microfluidic device capable of highly precise sample manipulation. The platform could control the fluid's path on a nanolitre-level, confine fluid to a 20 nL closed-loop, and create flow. This is all possible through a control layer housing pneumatic valves and a custom LabView® code. In Chapter 4, another level of sample control was introduced to isolate microbeads, a sieve valve. This valve confines the DNA on the microbeads to a 20 nL volume, and upon DNA elution in the closed-loop, a 25X concentration increase was observed. This device sheds light on only the beginning of the potential for microfluidic sample preparation.

5.2 Device Optimization

This work highlights the feasibility of sample preparation within microfluidic platforms. However, further work and optimization are required if paired with a nanopore sensor to increase the dynamic range. Firstly, the length of the target DNA should be increased. Research shows that longer DNA targets have enhanced binding to microbeads, resulting in higher elution efficiencies [148], [149]. The ratio of microbeads to µg of DNA should also be optimized. This thesis used 2X more beads than needed for DNA in each sample to ensure the most was captured. However, this ultimately led to a lower concentration increase because around half of the beads did not have had DNA bound, and not all of the beads in the initial binding solution were in the concentration loop. A better alternative would be to sort the microbeads with target DNA from the bare microbeads, perhaps using a difference in charge or size. Combining multiple concentration techniques, such as microbeads with dielectrophoresis, could

significantly increase this method. The effects of AZ photoresist reflow also complicate nanopore incorporation. Device 1 would be ideal for nanopore incorporation, as it could be integrated right below the fluid channel layer (***Figure 3-6***). Increased the channel heights at areas for valve closure, so the valves on this device do not seal fully. A new device design should be made where channel widths do not change so abruptly to remedy this. More consistent channel widths should reduce the adverse effects of reflow.

Another consideration is buffer compatibility with solid-state nanopore sensing. Solid-state nanopores require high salt concentrations for detection; however, many microbeads need a low salt elution buffer. The use of a photocleavable target has been considered because the target could be eluted into a nanopore compatible buffer system. However, validation could be a challenge, especially if using fluorescence microscopy, because of dye photobleaching. A salt mixer could be integrated with the device to incorporate microbeads that need low salt for target elution. The salt mixer would allow for a nanopore compatible buffer; however, it would decrease the concentration factor, which must be considered.

5.3 Future Applications

The presented research on a preconcentrating microfluidic device can be extended in many directions. One of the first upgrades could be replacing the sieve valve with another bead capture microtool. As the microbead column increases, the flow rate decreases. If a long bead column is required, it will take a long time for it to reach sufficient length and even longer to elute the target. This is not practical, especially in terms of diagnostic or point-of-care applications. Replacing the sieve valve with a screen or filter with a large surface area would help maintain flow while capturing a large number of beads. Functionalizing part of the channel to cause immobilization of beads could be another option. Incorporating a magnet to trap magnetic beads along the channel's top or bottom would still allow for flow.

The successful incorporation of a nanopore sensor to this device would widen its future applications even more. As previously discussed, fluorescence microscopy is not an ideal method for monitoring concentration or the presence of a target. Solid-state nanopores are

much more attractive as there are no photobleaching issues or no costly, sensitive fluorescent dyes needed. The integration of nanopores within microfluidics has been well developed, and microbead assays provide versatile methods for isolation. Combining both these methods would allow for a wide range of analytes to be targeted. Many different fields would benefit from a small chip capable of sample concentration and analyte detection, including diagnostics, food safety and environmental monitoring.

Another direction for this device could be automation and continuous sample concentration. The volume on this chip is rather small, but we could imagine taking the concentrated sample from the 20 nL loop and sending it to a holding chamber while another 20 nL is concentrated. After doing this process 100 times, there would be enough volume to use a Nanodrop for concentration determination, which could be valuable depending on the setting. Automation is always a useful tool, as this would allow personnel without rigorous training to operate the device. The user would just have to inject the sample, and sensors could be implemented, so once the bead column is an adequate length, the device can automatically perform the steps outlined in ***Figure 4-1***.

To summarize, the field of nanopore sensors and microfluidics holds a lot of promise for future applications, especially when integrated. Though it still has a long way to go, it has come very far in just a few decades.

Chapter 6 REFERENCES

[1] K. Lee *et al.*, "Recent Progress in Solid-State Nanopores," *Advanced Materials*, vol. 30, no. 42. Wiley-VCH Verlag, 18-Oct-2018, doi: 10.1002/adma.201704680.

[2] Z. Tang, D. Zhang, W. Cui, H. Zhang, W. Pang, and X. Duan, "Fabrications, Applications and Challenges of Solid-State Nanopores: A Mini Review," *Nanomaterials and Nanotechnology*, vol. 6. SAGE Publications Inc., 01-Jan-2016, doi: 10.5772/64015.

[3] M. Charron, K. Briggs, S. King, M. Waugh, and V. Tabard-Cossa, "Precise DNA Concentration Measurements with Nanopores by Controlled Counting," *Analytical Chemistry*, vol. 91, no. 19, pp. 12228–12237, Oct. 2019, doi: 10.1021/acs.analchem.9b01900.

[4] M. Wanunu, "Nanopores: A journey towards DNA sequencing," *Physics of Life Reviews*, vol. 9, no. 2. pp. 125–158, Jun-2012, doi: 10.1016/j.plrev.2012.05.010.

[5] M. D. Graham, "The Coulter Principle: Foundation of an industry," *JALA - Journal of the Association for Laboratory Automation*, vol. 8, no. 6, pp. 72–81, 2003, doi: 10.1016/S1535-5535(03)00023-6.

[6] A. Vembadi, A. Menachery, and M. A. Qasaimeh, "Cell Cytometry: Review and Perspective on Biotechnological Advances," *Frontiers in Bioengineering and Biotechnology*, vol. 7, no. JUN. Frontiers Media S.A., 2019, doi: 10.3389/fbioe.2019.00147.

[7] D. Deamer, M. Akeson, and D. Branton, "Three decades of nanopore sequencing," *Nature Biotechnology*, vol. 34, no. 5. Nature Publishing Group, pp. 518–524, 06-May-2016, doi: 10.1038/nbt.3423.

[8] F. Haque, J. Li, H. C. Wu, X. J. Liang, and P. Guo, "Solid-state and biological nanopore for real-time sensing of single chemical and sequencing of DNA," *Nano Today*, vol. 8, no. 1. Elsevier B.V., pp. 56–74, 2013, doi: 10.1016/j.nantod.2012.12.008.

[9] C. Danelon, C. Santschi, J. Brugger, and H. Vogel, "Fabrication and functionalization of nanochannels by electron-beam-induced silicon oxide deposition," *Langmuir*, vol. 22, no. 25, pp. 10711–10715, Dec. 2006, doi: 10.1021/la061321c.

[10] A. J. Storm, J. H. Chen, H. W. Zandbergen, and C. Dekker, "Translocation of double-strand DNA through a silicon oxide nanopore," *Physical Review E - Statistical, Nonlinear, and Soft Matter Physics*, vol. 71, no. 5, May 2005, doi: 10.1103/PhysRevE.71.051903.

[11] C. Ying *et al.*, "Formation of Single Nanopores with Diameters of 20-50 nm in Silicon Nitride Membranes Using Laser-Assisted Controlled Breakdown," *ACS Nano*, vol. 12, no. 11, pp. 11458–11470, Nov. 2018, doi: 10.1021/acsnano.8b06489.

[12] W. M. Zhang *et al.*, "Controllable shrinking and shaping of silicon nitride nanopores under electron irradiation," *Applied Physics Letters*, vol. 90, no. 16, 2007, doi: 10.1063/1.2723680.

[13] H. Kwok, K. Briggs, and V. Tabard-Cossa, "Nanopore fabrication by controlled dielectric breakdown," *PLoS ONE*, vol. 9, no. 3, Mar. 2014, doi: 10.1371/journal.pone.0092880.

[14] B. N. Miles, A. P. Ivanov, K. A. Wilson, F. Doğan, D. Japrung, and J. B. Edel, "Single molecule sensing with solid-state nanopores: Novel materials, methods, and applications," *Chemical Society Reviews*, vol. 42, no. 1. pp. 15–28, 07-Jan-2013, doi: 10.1039/c2cs35286a.

[15] T. Jain, R. J. S. Guerrero, C. A. Aguilar, and R. Karnik, “Integration of solid-state nanopores in microfluidic networks via transfer printing of suspended membranes,” *Analytical Chemistry*, vol. 85, no. 8, pp. 3871–3878, Apr. 2013, doi: 10.1021/ac302972c.
[16] S. Banerjee *et al.*, “Slowing DNA transport using graphene-DNA interactions,” *Advanced Functional Materials*, vol. 25, no. 6, pp. 936–946, Feb. 2015, doi: 10.1002/adfm.201403719.
[17] C. Cao *et al.*, “Single-molecule sensing of peptides and nucleic acids by engineered aerolysin nanopores,” *Nature Communications*, vol. 10, no. 1, Dec. 2019, doi: 10.1038/s41467-019-12690-9.
[18] T. Albrecht, T. Gibb, and P. Nuttall, *Ion Transport in Nanopores*. 2013.
[19] R. Tahvildari *et al.*, “Manipulating Electrical and Fluidic Access in Integrated Nanopore-Microfluidic Arrays Using Microvalves,” *Small*, vol. 13, no. 10, Mar. 2017, doi: 10.1002/smll.201602601.
[20] M. Wanunu, T. Dadosh, V. Ray, J. Jin, L. McReynolds, and M. Drndić, “Rapid electronic detection of probe-specific microRNAs using thin nanopore sensors,” *Nature Nanotechnology*, vol. 5, no. 11, pp. 807–814, 2010, doi: 10.1038/nnano.2010.202.
[21] C. Shasha, R. Y. Henley, D. H. Stoloff, K. D. Rynearson, T. Hermann, and M. Wanunu, “Nanopore-based conformational analysis of a viral RNA drug target,” *ACS Nano*, vol. 8, no. 6, pp. 6425–6430, Jun. 2014, doi: 10.1021/nn501969r.
[22] W. Li *et al.*, “Single protein molecule detection by glass nanopores,” *ACS Nano*, vol. 7, no. 5, pp. 4129–4134, May 2013, doi: 10.1021/nn4004567.
[23] N. Varongchayakul, J. Song, A. Meller, and M. W. Grinstaff, “Single-molecule protein sensing in a nanopore: a tutorial,” *Chemical Society reviews*, vol. 47, no. 23. NLM (Medline), pp. 8512–8524, 26-Nov-2018, doi: 10.1039/c8cs00106e.
[24] M. R. Pergande and S. M. Cologna, “Isoelectric point separations of peptides and proteins,” *Proteomes*, vol. 5, no. 1. MDPI AG, 01-Mar-2017, doi: 10.3390/proteomes5010004.
[25] M. Gershow and J. A. Golovchenko, “Recapturing and trapping single molecules with a solid-state nanopore,” *Nature Nanotechnology*, vol. 2, no. 12, pp. 775–779, 2007, doi: 10.1038/nnano.2007.381.
[26] J. Shim *et al.*, “Detection and quantification of methylation in DNA using solid-state nanopores,” *Scientific Reports*, vol. 3, 2013, doi: 10.1038/srep01389.
[27] E. Osman, “Integration of Droplet Microfluidics with a Nanopore Sensor,” 2019.
[28] A. Y. Grosberg and Y. Rabin, “DNA capture into a nanopore: Interplay of diffusion and electrohydrodynamics,” *Journal of Chemical Physics*, vol. 133, no. 16, Oct. 2010, doi: 10.1063/1.3495481.
[29] J. Nakane, M. Akeson, and A. Marziali, “Evaluation of nanopores as candidates for electronic analyte detection,” pp. 2592–2601, 2002.
[30] G. Ando, C. Hyun, J. Li, and T. Mitsui, “Directly observing the motion of DNA molecules near solid-state nanopores,” *ACS Nano*, vol. 6, no. 11, pp. 10090–10097, Nov. 2012, doi: 10.1021/nn303816w.
[31] M. Wanunu, W. Morrison, Y. Rabin, A. Y. Grosberg, and A. Meller, “Electrostatic focusing of unlabelled DNA into nanoscale pores using a salt gradient,” *Nature Nanotechnology*, vol. 5, no. 2, pp. 160–165, 2010, doi: 10.1038/nnano.2009.379.

[32] P. Rowghanian and A. Y. Grosberg, “Electrophoretic capture of a DNA chain into a nanopore,” *Physical Review E - Statistical, Nonlinear, and Soft Matter Physics*, vol. 87, no. 4, Apr. 2013, doi: 10.1103/PhysRevE.87.042722.

[33] K. J. Freedman, L. M. Otto, A. P. Ivanov, A. Barik, S. H. Oh, and J. B. Edel, “Nanopore sensing at ultra-low concentrations using single-molecule dielectrophoretic trapping,” *Nature Communications*, vol. 7, Jan. 2016, doi: 10.1038/ncomms10217.

[34] W. Si *et al.*, “Investigation on the interaction length and access resistance of a nanopore with an atomic force microscopy,” *Science China Technological Sciences*, vol. 60, no. 4, pp. 552–560, Apr. 2017, doi: 10.1007/s11431-016-0494-7.

[35] Y. Wu, R. D. Tilley, and J. J. Gooding, “Challenges and Solutions in Developing Ultrasensitive Biosensors,” *Journal of the American Chemical Society*, vol. 141, no. 3, pp. 1162–1170, Jan. 2019, doi: 10.1021/jacs.8b09397.

[36] A. Taj, A. Rehman, and S. Z. Bajwa, “4 Biomarkers and Their Role in Detection of Biomolecules,” 2020.

[37] A. A. Seyhan and C. Carini, “Are innovation and new technologies in precision medicine paving a new era in patients centric care?,” *Journal of Translational Medicine*, vol. 17, no. 1. BioMed Central, 05-Apr-2019, doi: 10.1186/s12967-019-1864-9.

[38] W. J. Locke *et al.*, “DNA Methylation Cancer Biomarkers: Translation to the Clinic,” *Frontiers in Genetics*, vol. 10. Frontiers Media S.A., 14-Nov-2019, doi: 10.3389/fgene.2019.01150.

[39] F. J. Enguita, “New promising circulating RNA biomarkers for early diagnosis of lung adenocarcinoma,” *Annals of Translational Medicine*, vol. 7, no. S3, pp. S130–S130, Jul. 2019, doi: 10.21037/atm.2019.05.70.

[40] Q. Zhou *et al.*, “Quantitative proteomics identifies brain acid soluble protein 1 (BASP1) as a prognostic biomarker candidate in pancreatic cancer tissue,” *EBioMedicine*, vol. 43, pp. 282–294, May 2019, doi: 10.1016/j.ebiom.2019.04.008.

[41] J. Z. Kubicek-Sutherland, D. M. Vu, H. M. Mendez, S. Jakhar, and H. Mukundan, “Detection of lipid and amphiphilic biomarkers for disease diagnostics,” *Biosensors*, vol. 7, no. 3. MDPI AG, 04-Jul-2017, doi: 10.3390/bios7030025.

[42] S. B. Nimse, M. D. Sonawane, K. S. Song, and T. Kim, “Biomarker detection technologies and future directions,” *Analyst*, vol. 141, no. 3, pp. 740–755, Feb. 2016, doi: 10.1039/c5an01790d.

[43] N. T. Ho, A. Fan, C. M. Klapperich, and M. Cabodi, “Sample concentration and purification for point-of-care diagnostics,” in *Proceedings of the Annual International Conference of the IEEE Engineering in Medicine and Biology Society, EMBS*, 2012, pp. 2396–2399, doi: 10.1109/EMBC.2012.6346446.

[44] R. Sy, R. E. Rothman, and S. Yang, “PCR-based diagnostics PCR-based diagnostics for infectious diseases: uses, limitations, and future applications in acute-care settings,” 2004. [Online]. Available: http://infection.thelancet.com.

[45] S. A. Byrnes and B. H. Weigl, “Selecting analytical biomarkers for diagnostic applications: a first principles approach,” *Expert Review of Molecular Diagnostics*, vol. 18, no. 1, pp. 19–26, Jan. 2018, doi: 10.1080/14737159.2018.1412258.

[46] H. Wei *et al.*, “Particle sorting using a porous membrane in a microfluidic device,” *Lab on a Chip*, vol. 11, no. 2, pp. 238–245, Jan. 2011, doi: 10.1039/c0lc00121j.

[47] N. Pamme, “Continuous flow separations in microfluidic devices,” *Lab on a Chip*, vol. 7, no. 12. Royal Society of Chemistry, pp. 1644–1659, 2007, doi: 10.1039/b712784g.

[48] J. Y. Zhang, J. Do, W. R. Premasiri, L. D. Ziegler, and C. M. Klapperich, “Rapid point-of-care concentration of bacteria in a disposable microfluidic device using meniscus dragging effect,” *Lab on a Chip*, vol. 10, no. 23, pp. 3265–3270, Dec. 2010, doi: 10.1039/c0lc00051e.

[49] P. R. C. Gascoyne and J. v. Vykoukal, “Dielectrophoresis-based sample handling in general-purpose programmable diagnostic instruments,” in *Proceedings of the IEEE*, 2004, vol. 92, no. 1, pp. 22–42, doi: 10.1109/JPROC.2003.820535.

[50] O. Bahadir, “Ion-Exchange Chromatography and Its Applications,” in *Column Chromatography*, InTech, 2013.

[51] H. Bordelon, P. K. Russ, D. W. Wright, and F. R. Haselton, “A Magnetic Bead-Based Method for Concentrating DNA from Human Urine for Downstream Detection,” *PLoS ONE*, vol. 8, no. 7, Jul. 2013, doi: 10.1371/journal.pone.0068369.

[52] S. Berensmeier, “Magnetic particles for the separation and purification of nucleic acids,” *Applied Microbiology and Biotechnology*, vol. 73, no. 3. pp. 495–504, Dec-2006, doi: 10.1007/s00253-006-0675-0.

[53] A. C. Moser and D. S. Hage, “Immunoaffinity chromatography: An introduction to applications and recent developments,” *Bioanalysis*, vol. 2, no. 4. pp. 769–790, Apr-2010, doi: 10.4155/bio.10.31.

[54] V. Mani, D. P. Wasalathanthri, A. A. Joshi, C. v. Kumar, and J. F. Rusling, “Highly efficient binding of paramagnetic beads bioconjugated with 100-000 or more antibodies to protein-coated surfaces,” *Analytical Chemistry*, vol. 84, no. 23, pp. 10485–10491, Dec. 2012, doi: 10.1021/ac3028257.

[55] S. S. Leong, S. P. Yeap, and J. K. Lim, “Working principle and application of magnetic separation for biomedical diagnostic at high- and low-field gradients,” *Interface Focus*, vol. 6, no. 6. Royal Society of London, 06-Dec-2016, doi: 10.1098/rsfs.2016.0048.

[56] N. Ali, R. D. C. P. Rampazzo, A. Di. T. Costa, and M. A. Krieger, “Current Nucleic Acid Extraction Methods and Their Implications to Point-of-Care Diagnostics,” *BioMed Research International*, vol. 2017. Hindawi Limited, 2017, doi: 10.1155/2017/9306564.

[57] M. Franzreb, M. Siemann-Herzberg, T. J. Hobley, and O. R. T. Thomas, “Protein purification using magnetic adsorbent particles,” *Applied Microbiology and Biotechnology*, vol. 70, no. 5. pp. 505–516, May-2006, doi: 10.1007/s00253-006-0344-3.

[58] C. M. Niemeyer, M. Adler, and R. Wacker, “Detecting antigens by quantitative immuno-PCR,” *Nature Protocols*, vol. 2, no. 8, pp. 1918–1930, Aug. 2007, doi: 10.1038/nprot.2007.267.

[59] J. Fu, L. Wu, Y. Qiao, J. Tu, and Z. Lu, “Microfluidic systems applied in solid-state nanopore sensors,” *Micromachines*, vol. 11, no. 3. MDPI AG, 01-Mar-2020, doi: 10.3390/mi11030332.

[60] K. J. Freedman, L. M. Otto, A. P. Ivanov, A. Barik, S. H. Oh, and J. B. Edel, “Nanopore sensing at ultra-low concentrations using single-molecule dielectrophoretic trapping,” *Nature Communications*, vol. 7, Jan. 2016, doi: 10.1038/ncomms10217.

[61] S. K. Fischer *et al.*, “Emerging Technologies to Increase Ligand Binding Assay Sensitivity,” *AAPS Journal*, vol. 17, no. 1, pp. 93–101, Jan. 2015, doi: 10.1208/s12248-014-9682-8.

[62] A. Nehra, S. Ahlawat, and K. P. Singh, “A biosensing expedition of nanopore: A review,” *Sensors and Actuators, B: Chemical*, vol. 284. Elsevier B.V., pp. 595–622, 01-Apr-2019, doi: 10.1016/j.snb.2018.12.143.

[63] J. Quick *et al.*, “Real-time, portable genome sequencing for Ebola surveillance,” *Nature*, vol. 530, no. 7589, pp. 228–232, Feb. 2016, doi: 10.1038/nature16996.
[64] L. E. Kafetzopoulou *et al.*, “Metagenomic sequencing at the epicenter of the Nigeria 2018 Lassa fever outbreak,” *Science*, vol. 363, no. 6422, pp. 74–77, Jan. 2019, doi: 10.1126/science.aau9343.
[65] S. W. Kowalczyk, D. B. Wells, A. Aksimentiev, and C. Dekker, “Slowing down DNA translocation through a nanopore in lithium chloride,” *Nano Letters*, vol. 12, no. 2, pp. 1038–1044, Feb. 2012, doi: 10.1021/nl204273h.
[66] B. M. Venkatesan and R. Bashir, “Nanopore sensors for nucleic acid analysis,” *Nature Nanotechnology*, vol. 6, no. 10. Nature Publishing Group, pp. 615–624, 2011, doi: 10.1038/nnano.2011.129.
[67] Z. Tang, B. Lu, Q. Zhao, J. Wang, K. Luo, and D. Yu, “Surface modification of solid-state nanopores for sticky-free translocation of single-stranded DNA,” *Small*, vol. 10, no. 21, pp. 4332–4339, Nov. 2014, doi: 10.1002/smll.201401091.
[68] I. Yanagi, K. Fujisaki, H. Hamamura, and K. I. Takeda, “Thickness-dependent dielectric breakdown and nanopore creation on sub-10-nm-thick SiN membranes in solution,” *Journal of Applied Physics*, vol. 121, no. 4, Jan. 2017, doi: 10.1063/1.4974286.
[69] M. J. Kim, M. Wanunu, D. C. Bell, and A. Meller, “Rapid fabrication of uniformly sized nanopores and nanopore arrays for parallel DNA analysis,” *Advanced Materials*, vol. 18, no. 23, pp. 3149–3153, Dec. 2006, doi: 10.1002/adma.200601191.
[70] J. Feng *et al.*, “Identification of single nucleotides in MoS 2 nanopores,” *Nature Nanotechnology*, vol. 10, no. 12, pp. 1070–1076, Dec. 2015, doi: 10.1038/nnano.2015.219.
[71] K. Venta *et al.*, “Differentiation of short, single-stranded DNA homopolymers in solid-state nanopores,” *ACS Nano*, vol. 7, no. 5, pp. 4629–4636, May 2013, doi: 10.1021/nn4014388.
[72] E. Beamish, V. Tabard-Cossa, and M. Godin, “Programmable DNA Nanoswitch Sensing with Solid-State Nanopores,” *ACS Sensors*, vol. 4, no. 9, pp. 2458–2464, Sep. 2019, doi: 10.1021/acssensors.9b01053.
[73] J. K. Rosenstein, M. Wanunu, C. A. Merchant, M. Drndic, and K. L. Shepard, “Integrated nanopore sensing platform with sub-microsecond temporal resolution,” *Nature Methods*, vol. 9, no. 5, pp. 487–492, May 2012, doi: 10.1038/nmeth.1932.
[74] J. Larkin, R. Y. Henley, M. Muthukumar, J. K. Rosenstein, and M. Wanunu, “High-bandwidth protein analysis using solid-state nanopores,” *Biophysical Journal*, vol. 106, no. 3, pp. 696–704, Feb. 2014, doi: 10.1016/j.bpj.2013.12.025.
[75] S. Shekar *et al.*, “Measurement of DNA translocation dynamics in a solid-state nanopore at 100 ns temporal resolution,” *Nano Letters*, vol. 16, no. 7, pp. 4483–4489, Jul. 2016, doi: 10.1021/acs.nanolett.6b01661.
[76] A. R. Chandrasekaran *et al.*, “Detection of cellular microRNAs with programmable DNA nanoswitches,” p. 334631, 2018, doi: 10.1101/334631.
[77] J. Li and D. S. Talaga, “The distribution of DNA translocation times in solid-state nanopores,” *Journal of Physics Condensed Matter*, vol. 22, no. 45, Nov. 2010, doi: 10.1088/0953-8984/22/45/454129.
[78] D. Fologea, J. Uplinger, B. Thomas, D. S. McNabb, and J. Li, “Slowing DNA translocation in a solid-state nanopore,” *Nano Letters*, vol. 5, no. 9, pp. 1734–1737, Sep. 2005, doi: 10.1021/nl051063o.

[79] C. Hyun, H. Kaur, R. Rollings, M. Xiao, and J. Li, “Threading immobilized DNA molecules through a solid-state nanopore at >100 μs per base rate,” *ACS Nano*, vol. 7, no. 7, pp. 5892–5900, Jul. 2013, doi: 10.1021/nn4012434.
[80] Y. He, M. Tsutsui, C. Fan, M. Taniguchi, and T. Kawai, “Controlling DNA translocation through gate modulation of nanopore wall surface charges,” in *ACS Nano*, 2011, vol. 5, no. 7, pp. 5509–5518, doi: 10.1021/nn201883b.
[81] M. A. Koussa, K. Halvorsen, A. Ward, and W. P. Wong, “DNA nanoswitches: A quantitative platform for gel-based biomolecular interaction analysis,” *Nature Methods*, vol. 12, no. 2, pp. 123–126, Jan. 2015, doi: 10.1038/nmeth.3209.
[82] R. Nouri, Z. Tang, and W. Guan, “Quantitative Analysis of Factors Affecting the Event Rate in Glass Nanopore Sensors,” *ACS Sensors*, vol. 4, no. 11, pp. 3007–3013, Nov. 2019, doi: 10.1021/acssensors.9b01540.
[83] D. J. Niedzwiecki, J. Grazul, and L. Movileanu, “Single-molecule observation of protein adsorption onto an inorganic surface,” *Journal of the American Chemical Society*, vol. 132, no. 31, pp. 10816–10822, Aug. 2010, doi: 10.1021/ja1026858.
[84] G. F. Schneider *et al.*, “Tailoring the hydrophobicity of graphene for its use as nanopores for DNA translocation,” *Nature Communications*, vol. 4, Oct. 2013, doi: 10.1038/ncomms3619.
[85] E. C. Yusko *et al.*, “Controlling protein translocation through nanopores with bio-inspired fluid walls,” *Nature Nanotechnology*, vol. 6, no. 4, pp. 253–260, 2011, doi: 10.1038/nnano.2011.12.
[86] M. C. Lim, M. H. Lee, K. B. Kim, T. J. Jeon, and Y. R. Kim, “A mask-free passivation process for low noise nanopore devices,” *Journal of Nanoscience and Nanotechnology*, vol. 15, no. 8, pp. 5971–5977, Aug. 2015, doi: 10.1166/jnn.2015.10500.
[87] C. R. Crick *et al.*, “Precise attoliter temperature control of nanopore sensors using a nanoplasmonic bullseye,” *Nano Letters*, vol. 15, no. 1, pp. 553–559, Jan. 2015, doi: 10.1021/nl504536j.
[88] K. Chuah *et al.*, “Nanopore blockade sensors for ultrasensitive detection of proteins in complex biological samples,” *Nature Communications*, vol. 10, no. 1, Dec. 2019, doi: 10.1038/s41467-019-10147-7.
[89] I. F. Pinto *et al.*, “The application of microbeads to microfluidic systems for enhanced detection and purification of biomolecules,” *Methods*, vol. 116, pp. 112–124, Mar. 2017, doi: 10.1016/j.ymeth.2016.12.005.
[90] Y. Liu *et al.*, “Microfluidic implementation of functional cytometric microbeads for improved multiplexed cytokine quantification,” *Biomicrofluidics*, vol. 12, no. 4, Jul. 2018, doi: 10.1063/1.5044449.
[91] E. Beamish, “Biomarker Assay Development and Sensing with Solid-State Nanopores.”
[92] A. Psifidi *et al.*, “Comparison of eleven methods for genomic DNA extraction suitable for large-scale whole-genome genotyping and long-term DNA banking using blood samples,” *PLoS ONE*, vol. 10, no. 1, Jan. 2015, doi: 10.1371/journal.pone.0115960.
[93] S. C. Tan and B. C. Yiap, “DNA, RNA, and protein extraction: The past and the present,” *Journal of Biomedicine and Biotechnology*, vol. 2009. 2009, doi: 10.1155/2009/574398.
[94] K. Kojima and O. Satoshi, “US Patent: Method for isolating and purifying nucleic acids,” 2002.

[95] Z. Barganska, M. Slebioda, and J. Namiesnik, “Determination of pesticide residues in honeybees using modified QUEChERS sample work-up and liquid chromatography-tandem mass spectrometry,” *Molecules*, vol. 19, no. 3, pp. 2911–2924, 2014, doi: 10.3390/molecules19032911.

[96] M. Sajid and C. Basheer, “Layered double hydroxides: Emerging sorbent materials for analytical extractions,” *TrAC - Trends in Analytical Chemistry*, vol. 75. Elsevier B.V., pp. 174–182, 01-Jan-2016, doi: 10.1016/j.trac.2015.06.010.

[97] A. R. Fontana, A. Camargo, L. D. Martinez, and J. C. Altamirano, “Dispersive solid-phase extraction as a simplified clean-up technique for biological sample extracts. Determination of polybrominated diphenyl ethers by gas chromatography-tandem mass spectrometry,” *Journal of Chromatography A*, vol. 1218, no. 18, pp. 2490–2496, May 2011, doi: 10.1016/j.chroma.2011.02.058.

[98] M. A. Farajzadeh, A. Yadeghari, and M. Abbaspour, “Dispersive solid phase extraction using magnetic nanoparticles performed in a narrow-bored tube for extraction of atorvastatin, losartan, and valsartan in plasma,” *Advanced Pharmaceutical Bulletin*, vol. 9, no. 1, pp. 138–146, 2019, doi: 10.15171/apb.2019.017.

[99] S. Gul, S. B. Khan, I. U. Rehman, M. A. Khan, and M. I. Khan, “A Comprehensive Review of Magnetic Nanomaterials Modern Day Theranostics,” *Frontiers in Materials*, vol. 6. Frontiers Media S.A., 31-Jul-2019, doi: 10.3389/fmats.2019.00179.

[100] J. Kudr *et al.*, “Magnetic nanoparticles: From design and synthesis to real world applications,” *Nanomaterials*, vol. 7, no. 9. MDPI AG, 01-Sep-2017, doi: 10.3390/nano7090243.

[101] P. E. Vandeventer, J. S. Lin, T. J. Zwang, A. Nadim, M. S. Johal, and A. Niemz, “Multiphasic DNA adsorption to silica surfaces under varying buffer, pH, and ionic strength conditions,” *Journal of Physical Chemistry B*, vol. 116, no. 19, pp. 5661–5670, May 2012, doi: 10.1021/jp3017776.

[102] K. A. Melzak, C. S. Sherwood, R. F. B. Turner, and C. A. Haynes, “Driving Forces for DNA Adsorption to Silica in Perchlorate Solutions merce identified the development of new tools for DNA,” 1996.

[103] T. H. Nguyen and M. Elimelech, “Plasmid DNA adsorption on silica: Kinetics and conformational changes in monovalent and divalent salts,” *Biomacromolecules*, vol. 8, no. 1, pp. 24–32, Jan. 2007, doi: 10.1021/bm0603948.

[104] S. Lindman, S. Linse, F. A. A. Mulder, and I. André, “pKa values for side-chain carboxyl groups of a PGB1 variant explain salt and pH-dependent stability,” *Biophysical Journal*, vol. 92, no. 1, pp. 257–266, 2007, doi: 10.1529/biophysj.106.088682.

[105] T. L. Hawkins, T. O’connor-Morin, A. Roy1, and C. Santillan, “DNA purification and isolation using a solid-phase,” 1994.

[106] A. Sarkar, H. W. Hou, A. E. Mahan, J. Han, and G. Alter, “Multiplexed Affinity-Based Separation of Proteins and Cells Using Inertial Microfluidics,” *Scientific Reports*, vol. 6, Mar. 2016, doi: 10.1038/srep23589.

[107] P. Brescia and P. Banks, “Analytical Performance of Nucleic Acid Micro-Volume Quantifi cation Using the Epoch ™ Spectrophotometer System,” Winooski, 2009. [Online]. Available: www.biotek.com.

[108] R. Friedrich, E. Rappold, C. Bogdan, and J. Held, “Comparative analysis of the wako B-glucan test and the fungitell assay for diagnosis of candidemia and Pneumocystis

jirovecii pneumonia," *Journal of Clinical Microbiology*, vol. 56, no. 9, Sep. 2018, doi: 10.1128/JCM.

[109] Y. Zhao *et al.*, "Lab-on-a-chip technologies for single-molecule studies," *Lab on a Chip*, vol. 13, no. 12. Royal Society of Chemistry, pp. 2183–2198, 21-Jun-2013, doi: 10.1039/c3lc90042h.

[110] R. Tahvildari, E. Beamish, V. Tabard-Cossa, and M. Godin, "Integrating nanopore sensors within microfluidic channel arrays using controlled breakdown," *Lab on a Chip*, vol. 15, no. 6, pp. 1407–1411, 2015, doi: 10.1039/c4lc01366b.

[111] A. Najafi Sohi, E. Beamish, V. Tabard-Cossa, and M. Godin, "DNA Capture by Nanopore Sensors under Flow," *Analytical Chemistry*, p. acs.analchem.9b05778, May 2020, doi: 10.1021/acs.analchem.9b05778.

[112] K. W. Oh and C. H. Ahn, "A review of microvalves," *Journal of Micromechanics and Microengineering*, vol. 16, no. 5, May 2006, doi: 10.1088/0960-1317/16/5/R01.

[113] V. Studer, G. Hang, A. Pandolfi, M. Ortiz, W. F. Anderson, and S. R. Quake, "Scaling properties of a low-actuation pressure microfluidic valve," *Journal of Applied Physics*, vol. 95, no. 1, pp. 393–398, Jan. 2004, doi: 10.1063/1.1629781.

[114] K. Brower, A. K. White, and P. M. Fordyce, "Multi-step variable height photolithography for valved multilayer microfluidic devices," *Journal of Visualized Experiments*, vol. 2017, no. 119, Jan. 2017, doi: 10.3791/55276.

[115] Z. J. Lian, S. Y. Hung, M. H. Shen, and H. Yang, "Rapid fabrication of semiellipsoid microlens using thermal reflow with two different photoresists," *Microelectronic Engineering*, vol. 115, pp. 46–50, Mar. 2014, doi: 10.1016/j.mee.2013.10.025.

[116] R. Tahvildari, "Integrating Solid-State Nanopore Sensors within Various Microfluidic Arrays for Single-Molecule Detection Solid-State Nanopore/Microfuidic Integrated Platforms for Bio Sensing View project," doi: 10.20381/ruor-20112.

[117] C. Weijie Beh, W. Zhou, and T.-H. Wang, "PDMS-Glass bonding using grafted polymeric adhesive-Alternative process flow for compatibility with patterned biological molecules," doi: 10.1039/b000000x/NIH.

[118] E. Jiménez-Díaz *et al.*, "Micro-macro: Selective integration of microfeatures inside low-cost macromolds for PDMS microfluidics fabrication," *Micromachines*, vol. 10, no. 9, Sep. 2019, doi: 10.3390/mi10090576.

[119] H. Lee, D. Koh, L. Xu, S. Row, S. T. Andreadis, and K. W. Oh, "A simple method for fabrication of microstructures using a PDMS stamp," *Micromachines*, vol. 7, no. 10, Oct. 2016, doi: 10.3390/mi7100173.

[120] S. Quake, J. Marcus, and C. Hansen, "US Patent: Microfluidic Sieve Valves," San Francisco, Oct. 2008.

[121] M. A. Unger, H.-P. Chou, T. Thorsen, A. Scherer, and S. R. Quake, "Monolithic Microfabricated Valves and Pumps by Multilayer Soft Lithography." [Online]. Available: http://science.sciencemag.org/.

[122] Y. N. Yang, S. K. Hsiung, and G. bin Lee, "A pneumatic micropump incorporated with a normally closed valve capable of generating a high pumping rate and a high back pressure," *Microfluidics and Nanofluidics*, vol. 6, no. 6, pp. 823–833, 2009, doi: 10.1007/s10404-008-0356-7.

[123] J. Xiang, Z. Cai, Y. Zhang, and W. Wang, "A micro-cam actuated linear peristaltic pump for microfluidic applications," *Sensors and Actuators, A: Physical*, vol. 251, pp. 20–25, Nov. 2016, doi: 10.1016/j.sna.2016.09.008.

[124] T. A. Duncombe, A. M. Tentori, and A. E. Herr, “Microfluidics: Reframing biological enquiry,” *Nature Reviews Molecular Cell Biology*, vol. 16, no. 9. Nature Publishing Group, pp. 554–567, 21-Aug-2015, doi: 10.1038/nrm4041.
[125] J. P. Grinias and R. T. Kennedy, “Advances in and prospects of microchip liquid chromatography,” *TrAC - Trends in Analytical Chemistry*, vol. 81. Elsevier B.V., pp. 110–117, 01-Aug-2016, doi: 10.1016/j.trac.2015.08.002.
[126] K. Ward and Z. H. Fan, “Mixing in microfluidic devices and enhancement methods,” *Journal of Micromechanics and Microengineering*, vol. 25, no. 9, Sep. 2015, doi: 10.1088/0960-1317/25/9/094001.
[127] M. H. Wu, S. bin Huang, Z. Cui, Z. Cui, and G. bin Lee, “Development of perfusion-based micro 3-D cell culture platform and its application for high throughput drug testing,” *Sensors and Actuators, B: Chemical*, vol. 129, no. 1, pp. 231–240, Jan. 2008, doi: 10.1016/j.snb.2007.07.145.
[128] T. N. Gerasimenko, O. v. Kindeeva, V. A. Petrov, A. I. Khaustov, and E. v. Trushkin, “Modelling and characterization of a pneumatically actuated peristaltic micropump,” Dec. 2016, doi: 10.1016/j.apm.2017.08.008.
[129] C. K. Byun, K. Abi-Samra, Y. K. Cho, and S. Takayama, “Pumps for microfluidic cell culture,” *Electrophoresis*, vol. 35, no. 2–3. pp. 245–257, 2014, doi: 10.1002/elps.201300205.
[130] H.-P. Chou, M. A. Unger, and S. R. Quake, “A Microfabricated Rotary Pump,” 2001. [Online]. Available: http://thebigone.caltech.edu/quake/.
[131] R. S. Lima *et al.*, “Sacrificial adhesive bonding: A powerful method for fabrication of glass microchips,” *Scientific Reports*, vol. 5, Aug. 2015, doi: 10.1038/srep13276.
[132] V. Studer, G. Hang, A. Pandolfi, M. Ortiz, W. F. Anderson, and S. R. Quake, “Scaling properties of a low-actuation pressure microfluidic valve,” *Journal of Applied Physics*, vol. 95, no. 1, pp. 393–398, Jan. 2004, doi: 10.1063/1.1629781.
[133] P. M. Fordyce, C. A. Diaz-Botia, J. L. Derisi, and R. Gomez-Sjoberg, “Systematic characterization of feature dimensions and closing pressures for microfluidic valves produced via photoresist reflow,” *Lab on a Chip*, vol. 12, no. 21, pp. 4287–4295, Nov. 2012, doi: 10.1039/c2lc40414a.
[134] B. Giri, B. Pandey, B. Neupane, and F. S. Ligler, “Signal amplification strategies for microfluidic immunoassays,” *TrAC - Trends in Analytical Chemistry*, vol. 79. Elsevier B.V., pp. 326–334, 01-May-2016, doi: 10.1016/j.trac.2015.10.021.
[135] J. M. Martel *et al.*, “Continuous Flow Microfluidic Bioparticle Concentrator,” *Scientific Reports*, vol. 5, Jun. 2015, doi: 10.1038/srep11300.
[136] Z. Ge, W. Wang, and C. Yang, “Rapid concentration of deoxyribonucleic acid via Joule heating induced temperature gradient focusing in poly-dimethylsiloxane microfluidic channel,” *Analytica Chimica Acta*, vol. 858, no. 1, pp. 91–97, 2015, doi: 10.1016/j.aca.2014.12.016.
[137] Y. Cong, S. Katipamula, T. Geng, S. A. Prost, K. Tang, and R. T. Kelly, “Electrokinetic sample preconcentration and hydrodynamic sample injection for microchip electrophoresis using a pneumatic microvalve,” *Electrophoresis*, vol. 37, no. 3, pp. 455–462, Feb. 2016, doi: 10.1002/elps.201500286.
[138] C. C. Lin, J. L. Hsu, and G. bin Lee, “Sample preconcentration in microfluidic devices,” *Microfluidics and Nanofluidics*, vol. 10, no. 3. pp. 481–511, Mar-2011, doi: 10.1007/s10404-010-0661-9.

[139] S. M. Azimi, G. Nixon, J. Ahern, and W. Balachandran, “A magnetic bead-based DNA extraction and purification microfluidic device,” *Microfluidics and Nanofluidics*, vol. 11, no. 2, pp. 157–165, Aug. 2011, doi: 10.1007/s10404-011-0782-9.
[140] Y. Xu, W. Zhang, P. Zeng, and Q. Cao, “A butyl methacrylate monolithic column prepared in-situ on a microfluidic chip and its applications,” *Sensors*, vol. 9, no. 5, pp. 3437–3446, Apr. 2009, doi: 10.3390/s90503437.
[141] W. Chang, T. Komazu, and T. Korenaga, “Fabrication of monolithic silica in microchannel as an adsorbent for preconcentration of VOCs,” *Analytical Letters*, vol. 41, no. 8, pp. 1468–1476, Jan. 2008, doi: 10.1080/00032710802119616.
[142] W. Liu, Z. Zhang, and Z. Liu, “Determination of β-lactam antibiotics in milk using micro-flow chemiluminescence system with on-line solid phase extraction,” *Analytica Chimica Acta*, vol. 592, no. 2, pp. 187–192, Jun. 2007, doi: 10.1016/j.aca.2007.04.027.
[143] S. J. Lee *et al.*, “Microslit on a chip: A simplified filter to capture circulating tumor cells enlarged with microbeads,” *PLoS ONE*, vol. 14, no. 10, Oct. 2019, doi: 10.1371/journal.pone.0223193.
[144] J. G. Kralj *et al.*, “T7-based linear amplification of low concentration mRNA samples using beads and microfluidics for global gene expression measurements,” *Lab on a Chip*, vol. 9, no. 7, pp. 917–924, 2009, doi: 10.1039/b811714d.
[145] S. Mukherji and D. Mondal, “Lab-on-chip (LOC) devices for point of care (POC) applications,” in *Medical Biosensors for Point of Care (POC) Applications*, Elsevier Inc., 2017, pp. 99–131.
[146] M. L. Chabinyc *et al.*, “An integrated fluorescence detection system in poly(dimethylsiloxane) for microfluidic applications,” *Analytical Chemistry*, vol. 73, no. 18, pp. 4491–4498, Sep. 2001, doi: 10.1021/ac010423z.
[147] N. B. Vicente, J. E. Diaz Zamboni, J. F. Adur, E. v. Paravani, and V. H. Casco, “Photobleaching correction in fluorescence microscopy images,” *Journal of Physics: Conference Series*, vol. 90, no. 1, Nov. 2007, doi: 10.1088/1742-6596/90/1/012068.
[148] M. Karwa, D. Hahn, and S. Mitra, “A sol-gel immobilization of nano and micron size sorbents in poly(dimethylsiloxane) (PDMS) microchannels for microscale solid phase extraction (SPE),” *Analytica Chimica Acta*, vol. 546, no. 1, pp. 22–29, Aug. 2005, doi: 10.1016/j.aca.2005.05.029.
[149] R. Zhong *et al.*, “Fabrication of two-weir structure-based packed columns for on-chip solid-phase extraction of DNA,” *Electrophoresis*, vol. 28, no. 16, pp. 2920–2926, Aug. 2007, doi: 10.1002/elps.200600604.

APPENDIX

Determining the number of beads needed to capture DNA in sample

Amount of DNA in Chapter 2 experiments:

The binding capacity of MagSi-DNA COOH 3.0 is 15µg/mg, provided by amsbio (https://www.amsbio.com/magsi-magnetic-beads-genomics/). Based on this, 5µL of MagSi-DNA 3.0 COOH beads can bind 1.5 µg of 50 base-pair DNA. 25µL of 30ng/µL 50 base-pair DNA contains 750ng DNA, so the beads are in excess.

$$5\ \mu L\ bead\ solution\ \frac{20\ mg\ beads}{mL\ bead\ solution} \times \frac{1\ mL}{1000\ \mu L} = 0.1\ mg\ beads$$

$$0.1\ mg\ beads\ \times \frac{15\ \mu g\ DNA}{mg\ beads} = 1.5\ \mu g$$

Amount of DNA in Chapter 4 experiments:

10ng/µL of DNA in 50 µL contains 500ng of DNA. 1.6 nL of beads would be needed to bind that amount DNA, 3 nL was used to ensure beads were in excess.

Determining the length of bead column:

To determine the bead column's length, work backwards from the concentration that needs to be achieved. Because the end goal of this project is to improve nanopore sensing, the final concentration should be a concentration that is optimal for nanopore detection. Tahvildari et al use 750ng/µL as a concentration for DNA samples of varying lengths (100bp-10kbp) for nanopore detection [19]. From experiments in Chapter 2, 40% of original DNA is eluted off of the beads. The volume of the closed-loop in the microfluidic device is 20nL.

$$Amount\ of\ DNA\ \ in\ loop = concentration\ \times\ volume$$

$$= 750\frac{ng}{\mu L} \times\ 20\ nL\ \times\ \frac{1\ \mu L}{1000\ nL}$$

$$= 15\ ng$$

To achieve a concentration of 750 ng/uL, 15 ng of DNA needs to be eluted off of the beads. Based on experimental results from Chapter 2, 15ng is only 40% of total DNA on the beads, so the beads need to have 37.5 ng of DNA bound to elute 40% = 15 ng.

Next is to determine how many beads are needed to bind 37.5 ng of DNA. MagSi DNA COOH 3.0 stat sheet (https://www.amsbio.com/magsi-magnetic-beads-genomics/) says the DNA binding capacity of the beads is 15 µg DNA/mg bead.

$$37.5\ ng\ DNA\ \times \frac{1\ \mu g}{1000\ ng} \times \frac{1\ mg\ beads}{15\ \mu g\ DNA} = 0.025\ mg\ beads$$

0.025 mg of beads are needed to bind 37.5 ng of DNA. How many beads are in 0025 mg of beads? The diameter of MagSi DNA COOH 3.0 beads is 3.0 µm, so assuming beads are relatively spherical*:

$$Volume\ of\ 1\ bead * = \frac{4}{3}\pi r^3$$
$$= 14.14\ \mu m^3$$

Bead density is 1.6 g/cm^{3,} so to find the weight of one bead:

$$1.6\frac{g}{cm^3} \times \frac{1000\ mg}{1\ g} \times \frac{1\ cm^3}{10^{12}\mu m^3} \times 14.14\ \mu m^3 = 2.26 \times 10^{-8}\ mg$$

So now to determine how many beads are in 0.025 mg:

$$\frac{0.025}{2.26 \times 10^{-8}} = 110\ 524\ beads$$

Next, it is important to know approximately how much volume this will take up in the device. The density of random sphere packing is 0.64. Meaning there is 0.36 added space for random sphere packing.

$$110\,524\ beads\ \times\ 14.14um^3 \times \frac{0.000001\ nL}{1\ um^3} = 1.56\ nL$$

$$1.56\ nL \times\ 1.36 = 2.1\ nL$$

Based on results from Chapter 2, the bead column would need to be a minimum of 2.1 nL in the microfluidic device.

Expected concentration increase:

Bead column volume:

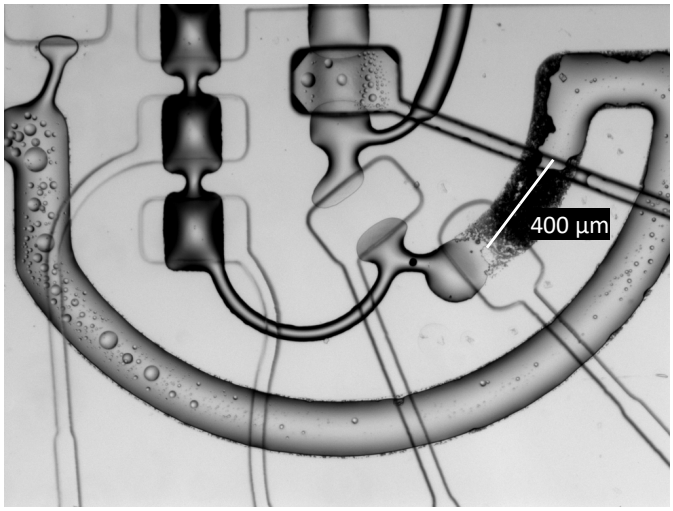

Figure 6-1: Length of bead column.

$$Volume\ half\ ellipse = \frac{\left(\frac{4}{3}\pi\ l\ w\ h\right)}{2}$$

$$= \frac{\frac{4}{3}\pi\ 300\ \mu m\ (length) \times\ 200\ \mu m(width) \times\ 20\mu m\ (height)}{2}$$

$$= 2513274\ \mu m^3\ \frac{0.000001\ nL}{\mu m^3}$$

$$= 2.5\ nL$$

Number of beads in 2.5 nL:

Volume of one bead= 14.14μm^3= 1.414 x 10^{-5} nL

Volume that is full of beads = 0.64 x 2.5 nL= 1.6 nL

$$\frac{1.6\ nL}{1.414\ \times\ 10^{-5}} = 113\ 754\ beads$$

Weight of 113 754 beads = 0.00257 mg

Amount of DNA that kind bind:

$$0.00257mg\ \times \frac{15\ ug\ DNA}{mg\ beads} = 0.0386\ mg\ =\ 38.6ng$$

*Assume 40% elution:

$$38.6\ ng\ \times\ 0.4 = 15.44\ ng\ eluted$$

$$\frac{15.44\ ng}{20\ nL} = \frac{0.772\ ng}{nL} = \frac{772\ ng}{\mu L}$$

The expected DNA concentration is 772 ng/uL, assuming all microbeads have DNA, and 40% is eluted.

However, because the microbeads were 2X in excess, a better assumption may be that only 50% of beads have DNA bound, in which case:

113 745 beads/ 2= 56 872 beads have DNA

Weight of 56 872 beads = 0.00129 mg

Amount of DNA that kind bind:

$$0.00129mg\ \times \frac{15\ ug\ DNA}{mg\ beads} = 0.0194\ mg\ =\ 19.35\ ng$$

*Assume 40% elution:

$$19.35\ ng\ \times\ 0.4 = 7.74\ ng\ eluted$$

$$\frac{7.74\ ng}{20\ nL} = \frac{0.387\ ng}{nL} = \frac{387\ ng}{\mu L}$$

The expected DNA concentration should be less than 387 ng/uL, after considering less than half of the microbeads may have DNA, and 40% will be eluted.